REPORT DOCUMENTATION PAGE

Form Approved
OMB No. 0704-0188

AD-A227 733

1. AGENCY USE ONLY *(Leave blank)*	2. REPORT DATE 1990	3. REPORT TYPE AND DATES COVERED Thesis/Dissertation

4. TITLE AND SUBTITLE
Fine Scale Analysis of the Kinematic, Dynamic and Thermodynamic Features of a Multiple Microburst-Producing Storm

5. FUNDING NUMBERS

6. AUTHOR(S)
Bradley Todd Regan

7. PERFORMING ORGANIZATION NAME(S) AND ADDRESS(ES)
AFIT Student at: Saint Louis Universtiy

8. PERFORMING ORGANIZATION REPORT NUMBER
AFIT/CI/CIA -90-083

9. SPONSORING/MONITORING AGENCY NAME(S) AND ADDRESS(ES)
AFIT/CI
Wright-Patterson AFB OH 45433

10. SPONSORING/MONITORING AGENCY REPORT NUMBER

11. SUPPLEMENTARY NOTES

12a. DISTRIBUTION/AVAILABILITY STATEMENT
Approved for Public Release IAW AFR 190-1
Distribution Unlimited
ERNEST A. HAYGOOD, 1st Lt, USAF
Executive Officer, Civilian Institution Programs

12b. DISTRIBUTION CODE

13. ABSTRACT *(Maximum 200 words)*

DTIC
ELECTE
OCT. 23 1990
S
B
D

14. SUBJECT TERMS	15. NUMBER OF PAGES 103
	16. PRICE CODE

17. SECURITY CLASSIFICATION OF REPORT UNCLASSIFIED	18. SECURITY CLASSIFICATION OF THIS PAGE	19. SECURITY CLASSIFICATION OF ABSTRACT	20. LIMITATION OF ABSTRACT

Standard Form 298 (Rev 2-89)

FINE SCALE ANALYSIS OF THE KINEMATIC, DYNAMIC

AND THERMODYNAMIC FEATURES OF A MULTIPLE

MICROBURST-PRODUCING STORM

Bradley Todd Regan, B.S.

A Digest Presented to the Faculty of the Graduate School
of Saint Louis University in Partial Fulfillment of
the Requirements for the Degree of
Master of Science (Research)

1990

COMMITTEE IN CHARGE OF CANDIDACY:

Professor Yeong-Jer Lin,
          Chairperson and Advisor

Associate Professor Robert W. Pasken

Assistant Professor Lawrence Coy

i

I dedicate the work herein to the Lord God, whom makes
all things possible to include the universal oneness of life.
Further dedication for this thesis goes to each of my
parents for their patience and courage throughout my
trials and to my immediate family, wife and children,
for their unending support morally, physically and
spiritually in the pursuit of my endeavors. Additional
dedication belongs to my loving brother for the bonds we
share and his exemplary standards toward responsibility.

horizontal spacing. Five layers existed in the vertical ranging from 0.25 to 1.25 km. Vertical velocities were calculated from the anelastic continuity equation by integrating upward from the surface. Thermodynamic retrieval was employed to retrieve fields of perturbation pressure and temperature from the Doppler derived winds using the three momentum equations. Data set comparisons yield conclusive information on microburst evolution and its planetary boundary layer interaction. An optimum horizontal grid spacing for use in Doppler analysis is also proposed.

ACKNOWLEDGEMENTS

viduals as yet unidentified, responsible for special inputs and personal integrities which helped to shape my character and develop my personality which has made my complete academic performance possible.

TABLE OF CONTENTS ·

LIST OF TABLES

LIST OF FIGURES

1. INTRODUCTION

Microbursts are typifed by extreme low-level wind shear (LLWS) and action/interaction both with and within the planetary boundary layer (PBL). Fujita (1976) first developed the term "microburst" to place emphasis upon its small scale nature (meso-γ) with a horizontal outflow diameter of less than 4 kilometers (km). The Joint Airport Weather Studies (JAWS) field project, conducted in summer of 1982 near Denver's Stapleton International Airport, focused on this deadly aviation hazard. Based on over 70 recorded events of microburst phenomena during JAWS, McCarthy et al. (1984) and Wilson et al. (1984) found that a typical microburst has a horizontal dimension of 1-3 km, a lifetime of 5-15 minutes (with period of most severe shear 2-4 minutes), an average wind differential of 25 m s^{-1} (maximum wind differential observed by Doppler radar was found to be 48 m s^{-1}) and a frequency of occurrence of 1.5 per day.

McCarthy (1984) explained that a microburst is most dangerous to aviation activities in close proximity to the ground; e.g., in that an aircraft on takeoff or landing with a microburst in progress first encounters an increasing headwind (pilot adjusts by increasing the throttle) next, an intense downdraft (pilot raises pitch upward) and finally, a dangerously strong tailwind (pilot is unable to react, the plane stalls, losing its lift and incapable of producing necessary thrust to maintain flight falls to the ground). The complete encounter lasts only moments with the result of loss in aircraft performance and quite often human fatalities. Figure 1.1 illustrates microburst phenomena

1

DIGEST

The Joint Airport Weather Studies (JAWS) project, designed to investigate low-level wind shear (LLWS) and its impact on aviation, provides abundant knowledge toward the phenomena of microbursts. Observational data collected by Doppler radar during the experiment is providing a better understanding of microburst/LLWS struture and Doppler analysis techniques. This understanding is important because deployment of Doppler radar at the national level, makes it the principle instrument toward regional (meso-scale) FORCASTING!

Microbursts are multi-faceted features of some thunderstorms and occur under a myriad of circumstances. Meteorologists are studying their history, evolution and outcome to glean insight into microburst. Microburst detection, warning, notification and general aviation education are becoming paramount issues in light of todays ever increasing air travel. The atmospheric state at the time of the microburst and boundary layer interaction exemplify the planetary cascade of energy as it occurs daily. Studies of this kind are necessary to focus attention upon the consequential impacts of these weather phenomena.

Data are presented for several microburst events which occurred on 5 August 1982. Kinematic, dynamic, and thermodynamic structures of these storms were investigated using Doppler data collected during JAWS. Fields of storm-relative wind and reflectivity were derived using the objective analysis scheme with 0.25 km horizontal grid spacing and compared with a previous study which used 0.5 km
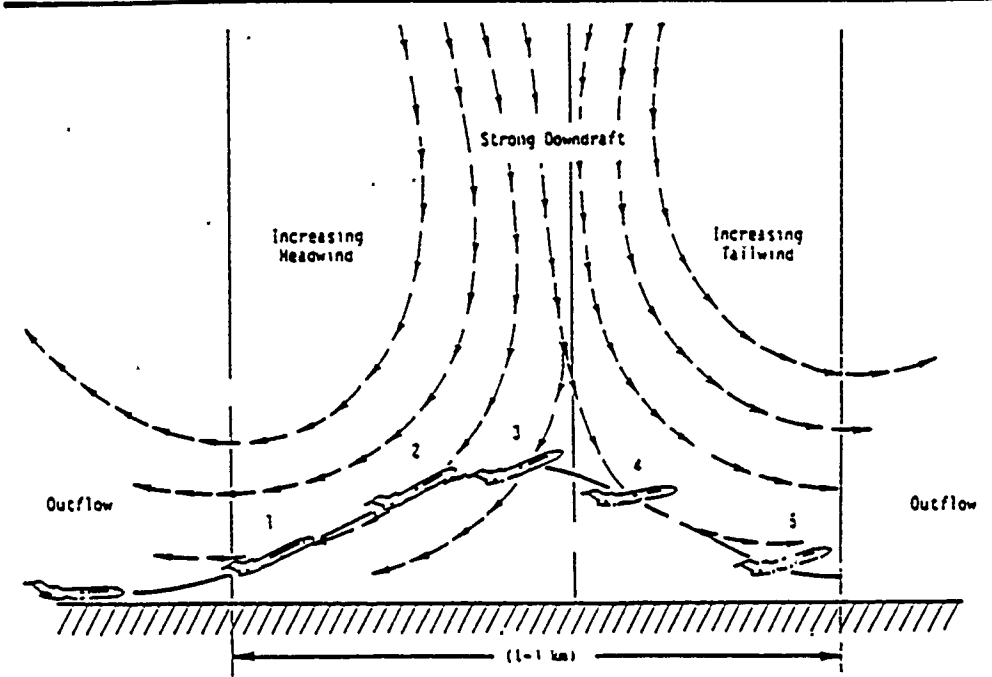
Fig. 1.1 Simulated microburst situation as it
impacts an aircraft in flight. The airplane
first encounters a headwind and experiences
increasing performance (1); this is followed
in short succession by a decreasing headwind
(2); a downdraft (3), and finally a strong
tailwind (4), where 2 through 5 all result in
decreasing performance of the airplane.
Position (5) represents an extreme situation
just prior to impact. (From Frost et
al.,(1984).

2

and its impact on aircraft in flight.

McCarthy and Serafin (1984) stated that Pan American flight #759 fell victim to microburst 9 July 1982 while attempting to takeoff from New Orleans International Airport, killing all 145 persons aboard and eight individuals on the ground. Additionally, McCarthy (1984) noted that microbursts have been blamed for at least 32 accidents/incidents globally since 1964 with a total of 500 deaths (Tables 1.1 and 1.2). McCarthy and Serafin (1984) emphasized that increased pilot education (films and lectures) and training/awareness (cockpit recognition, procedures and avoidance) along with improved technologies (advanced sensing low-level wind shear systems) are necessary to safely cope with microburst as an aviation hazard, regardless of their often benign appearance.

1.1 Joint Airport Weather Studies

The JAWS field project was a joint venture between scientists from the National Center for Atmospheric Research (NCAR) and the University of Chicago. McCarthy et al. (1982) discussed the primary objectives as follows: first, JAWS was designed to investigate the fine scale structure of thunderstorm dynamics and kinematics within the airport vicinity; second, to study LLWS and its impact on aviation activities and third, to employ and assess new technologies and sensing devices (both remote and active) as to their affectiveness in the detection, warning and display/notification of microburst/LLWS events. McCarthy (1984) stated another principle objective of the JAWS pro-

Table 1.1

Aircraft accidents and incidents related to low-altitude wind shear (1964-1982) (From McCarthy et al., 1984).

No	Year & Date	Time (LST)	Location	Airline Flt No (Aircraft type)	T/O or L(X) (Runway)	Fat/Inj	Wind Shear Experienced	Weather Systems
1	1964 MAR 01	1125	Lake Tahoe NV	Paradise 901A (L-1049)	L(X) ...	85/0	During climbout after a missed approach	Strong mountain lee wave during snowstorm
2	1964 JUL 01	2134	JFK New York NY	AA 64 (B-720B)	L(X) 31R	0/0	Windshift from headwind to crosswind	Thunderstorm with a sharp pressure rise
3	1965 MAR 17	1858	Kansas City MO	TWA 407 (B-727)	L(X) 36	0/0	Wind direction change on final, 310°-21kts to 280°-22kts	Unstable moist air
4	1968 JUN 08	1351	Salt Lake City UT	UAL 8327 (B-727)	L(X) 34L	0/1	260°-13kts at 1351 to 280°-12kts at 1354	Heavy thunderstorm with suspected gust front
5	1970 JUL 20	1136	Naha AB Okinawa	FFLY T1O 15 (DC-8)	L(X) 18	4/0	10kt tailwind near threshold	Heavy rainshower one mile in diameter
6	1970 DEC 10	1926	St Thomas VI	Carib.Air (CV-640)	L(X) 09	NA	Landing in 080°-20kts wind	Lee side flow in rainshower
7	1971 JAN 04	1832	LGA New York NY	FAA N-7 (DC-3)	L(X) 04	0/2	Tailwind changed into headwind.	Frontal Shear
8	1972 MAY 18	1121	Ft Lauderdale Fl.	EAL 316 (DC-9)	L(X) 09L	0/3	160°-10kts at 1418 to 130°-12kts at 1426	Heavy thunderstorm
9	1972 JUL 26	1606	New Orleans LA	NA 32 (B-727)	L(X) 28	0/0	IAS dropped 162 to 122kts	Intense rainstorm and thunderstorm
10	1972 DEC 12	2256	JFK New York NY	TWA 669 (B-707)	L(X) 04R	0/0	42kt tailwind at 1500Y to 5kt headwind at the surface	Frontal shear; Fog and drizzle
11	1973 MAR 03	1250	Wichita KS	TWA 315 (B-727)	L(X) 19R	0/0	100°-10kts at 1240 00 to 170°-10kts to 070°-10kts at 1249:10	Thunderstorm
12	1973 JUN 13	1403	ORD Chicago IL	Airlift 105 (DC 8)	L(X) 22R	0/0	Estimated downdraft 30fps at 3000Y, 13fps at 500' AGL	Heavy rainstorm
13	1973 JUL 23	1613	St Louis MO	OZ 809 (F11-227B)	L(X) 30L	38/6	Up- and downdrafts	Outflow shear; Thunderstorm, sharp pressure rise
14	1973 NOV 27	1851	Chattanooga TN	DL 516 (DC-9)	L(X) 20	0/12	Low-altitude wind shear	Outflow shear; Thunderstorm outflow

Table 1.2

Same as Table 1.1 (continuation)

#	Year	Date	Location	Flight (Aircraft)	Runway	Fatal/Inj	Wind	Description
15	1973	DEC 17	1913	Boston MA	Iberia 933 (DC-10)	●LDG 33L	0/16	200°-24kts at 500'; 260°-17kts at 200', 315°-08kts at surface	Frontal shear; Rain and fog
16	1974	JAN 30	2301	Pago Pago SAMOA	PAA 806 (B-707)	●LDG 05	96/3	Decreasing headwind and/or downdraft during the final 4 seconds	Outflow shear; Heavy rain shower
17	1975	JUN 24	1857	JFK New York NY	EAL 902 (L-1011)	OLDG 22L	—	8kts headwind to 6kts tailwind with 20fps downdraft	Small downburst or microburst; Strong thunderstorm
18	1975	JUN 24	1505	JFK New York NY	EAL 66 (B-727)	●LDG 22L	112/12	14kts headwind to 1kt headwind with 21fps downdraft	Small downburst or microburst; outflow shear; Strong thunderstorm
19	1975	AUG 07	1911	Denver CO	CO 426 (B-727)	●T/O 35L	0/15	IAS decreased 158 to 116kts in 5 seconds	Small downburst or microburst; Outflow shear; Thunderstorm
20	1975	NOV 12	2032	Raleigh NC	EAL 576 (B-727)	●LDG 23	0/1	10° windshift, gust up to 20kts	3 inch per hour rain fall rate
21	1975	DEC 31	1056	Greer SC	EAL (DC-9)	●LDG 03	0/0	200° change in wind direction	Light rain and fog
22	1976	JUN 23	1612	Philadelphia PA	AL 121 (DC-9)	●LDG 27R	0/87	65kts headwind to 20kts tailwind	Microburst; Outflow shear; Fast-moving thunderstorm
23	1976	DEC 12	2326	Cape May NJ	Atl City 977 (DHC-6)	●LDG 19	3/1	Gust to 50kts	Frontal shear
24	1977	JUN 03	1250	Tucson AZ	CO 63 (B-727)	●T/O 21	0/0	30kts headwind to 30kts tailwind	Microburst; Outflow shear; Downdraft in thunderstorm
25	1979	AUG 22	1012	Atlanta GA	EAL 693 (B727)	OLDG 27L	—	strong downdraft and headwind	Microburst; Thunderstorm rainshower
26	1982	JUL 09	1509	New Orleans LA	PAA 759 (B-727)	●T/O 10	153/9	Headwind tailwind and downdraft shear	Microburst with heavy rain
27	1982	JUL 28	1521	LGA New York NY	TWA 524 (B-727)	OLDG 22	—	Severe wind shear at 20-100' AGL	Strong thunderstorm with gusty winds

TOTAL: ●21 Accidents; O3 Incidents; 491 Fatalities / 206 Injuries

ject was to fully establish the three-dimensional, evolutionary structure of microburst phenomena.

The JAWS meteorological network consisted of three Doppler radars (NCAR's CP-2, CP-3 and CP-4), 27 portable automated mesonet (PAM) stations, one low level wind shear alerting system (LLWSAS), two CO_2 lidar (vertically pointing) radars and five research aircraft (Fig. 1.2). Wilson et al. (1984) detected over 70 microburst events via Doppler radar during JAWS. However, within the same period Fujita and Wakimoto (1983) identified 186 microbursts using PAM data. Based on the variety of recorded events and subsequent case studies, these researchers concluded that microbursts may occur under a multitude of synoptic conditions with emphasis placed not only on macro-scale convective triggers but, also on localized terrain induced forcing mechanisms like orographic uplift or diurnal/nocturnal changes. McCarthy and Wilson (1984) noted that LLWS/microbursts may occur in association with sea breeze circulations, airmass boundaries or fronts, strong winds blowing over rough terrain or convective storms.

Roberts and Wilson (1984) noted in all cases convergent flow aloft was a prominent feature in diagnosing microburst occurrence. Hjelmfelt (1984) discovered strong conditional instability aloft is typical of large microburst producing storms. Kessinger et al. (1984) found that strong small-scale downdrafts develop in close proximity to misocyclone circulations. McCarthy et al. (1984) verified that rotation aloft, weak echo regions (eroding areas) or notching and descending precipita-

JAWS NETWORK 1982
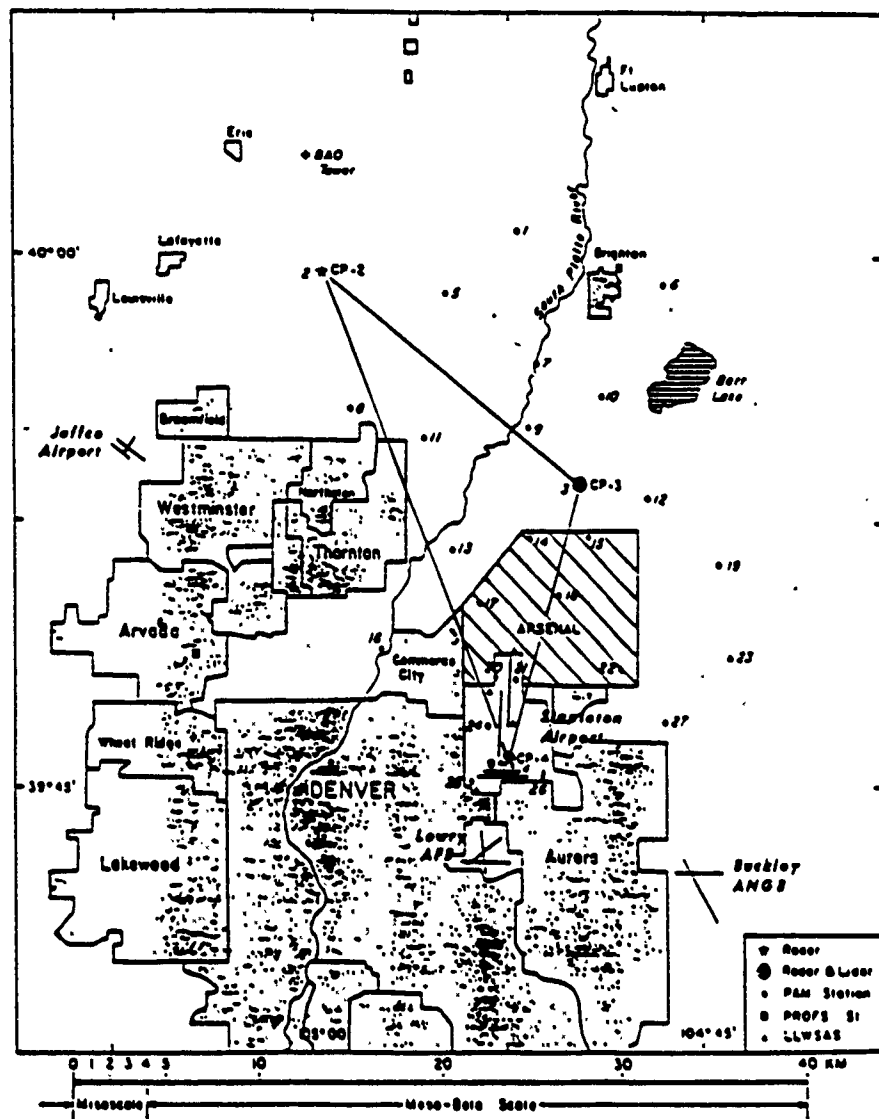
Fig. 1.2 JAWS meteorological network illustrating facilities situated within the vicinity of Denver's Stapleton International Airport (From McCarthy et al., 1983).

tion cores are all precursor signatures toward microburst phenomena. McCarthy and Serafin (1984) noted that microbursts can occur in association with thunderstorms/heavy rain situations or with weak convection containing verga and radar reflectivities at or below 25 dBZ. McCarthy (1984) found the most common microburst forcing mechanism seen in JAWS was cooling from evaporation, above or below the cloud base thus enhancing the production of negative boyancy. Roberts and Wilson (1984) found that soundings typical of mid-level moisture, dry subcloud regions and unstable nearly adiabatic lapse rates are indicative of convection and possible microburst formation.

Srivastava (1985) explained evaporative cooling is the most pronounced and significant parameter in initiating and enhancing a downdraft. Lin et al. (1987) noted the presence of microburst in the lower layers produces strong wind shear in all directions, which, in turn, strengthens the turbulent transfer of momentum throughout the layers. Further, Lin and Hughes (1987) found horizontal perturbation pressure gradients responsible for sustaining the strong diverging flow across the microburst. Lin (1988) stated the perturbation pressure force is an acceleration force driving the momentum transfer within the downdraft which acts to formulate a mesohigh at the microburst center and initiate meso lows upon its outskirts.

Boundary layer and free atmosphere interactions may be studied in detail using shallow volume scans of Doppler Radars. Lin and Hughes (1987) found that a meso-high pressure existed at the microburst/downdraft center with meso-low pressure being present

upon its flanks. Data comparison with other microburst events at different time periods indicate secondary circulations exist which provide positive feedback to further spawn and drive collectively microburst/misocyclone/gust front phenomenon. Further, Kessinger et al. (1984), Lin and Coover (1988) and Lapointe (1989) found wind rotors to exist within the boundary layer and upwind of downburst phenomena along with misocyclones at approximately 1 km.

McCarthy and Wilson (1984) showed that as a microburst/downdraft impinges upon the ground, it spreads out quasi-horizontally in accordance with mass continuity (Fig. 1.3). Research by McCarthy and Wilson (1984) and Hjelmfelt et al. (1984) noted that microbursts are often associated with descending precipitation shafts, in which evaporative cooling from precipitation initiates negative boyancy production. Hjelmfelt (1984) explained that soundings typical of microburst phenomena are characterized by a very dry and unstable PBL with a particularly dry layer near the sub-cloud base and conditional instability extending throughout the remainder of the troposphere into the tropopause.

McCarthy and Wilson (1984) discussed particular forcing mechanisms which govern microburst formation; subcloud cooling from evaporating precipitation, cooling from melting (shedding from melting hail), frictional drag from falling precipitation, dynamically induced vertical pressure gradients and downward transport of horizontal momentum. Additionally, Hjelmfelt (1984) showed that precipitation loading may also play an important role along with other forcing
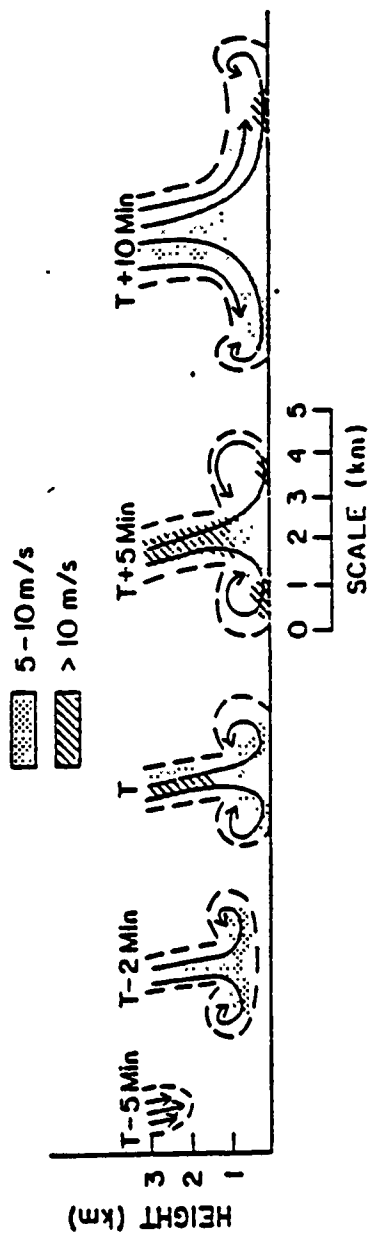
Fig. 1.3 Vertical cross section of the evolution of the microburst wind field based on JAWS data. T is the time of initial divergence at the surface. The shading refers to the vector wind speeds. (From Wilson et al., 1984).

mechanisms responsible for microburst. Also, Brown et al. (1984) noted that latent heat of melting/shedding hail will counter-act compressional warming.

Elmore and McCarthy (1984) studied the kinematics and flow fields of JAWS microbursts. Lin and Hughes (1987) and Lin et al. (1987) examined the kinematic, dynamic and thermodynamic properties of microburst using Gal-Chen's (1978) thermodynamic retrieval method. McCarthy et al. (1984) examined several intense (14 July 82) microburst events and captured picture perfect a vertical cross-section of the phenomena (Fig. 1.4). Lin and Condray (1987) studied the momentum flux of a JAWS microburst, Lin (1988) examined the eddy kinetic energy budget of a microburst-producing storm, Hughes (1987) focused on microburst structural features, Lapointe (1989) and Kessinger et al. (1984) examined circulation/rotation centers of JAWS microburst and McNamee (1989) included local pressure tendencies to improve microburst dynamic analysis. Finally, Coover (1988) analyzed the kinematic, dynamic and thermodynamic properties of a JAWS microburst-producing storm using 500 m horizontal grid spacing.

(a)

HORIZONTAL

10,000 ft

→30m/s

DISTANCE SOUTH OF CP-2 (km)

DISTANCE EAST OF CP-2 (km)

(b).

VERTICAL

→15 M/S

HEIGHT (km)

DISTANCE EAST OF CP-2 (km)
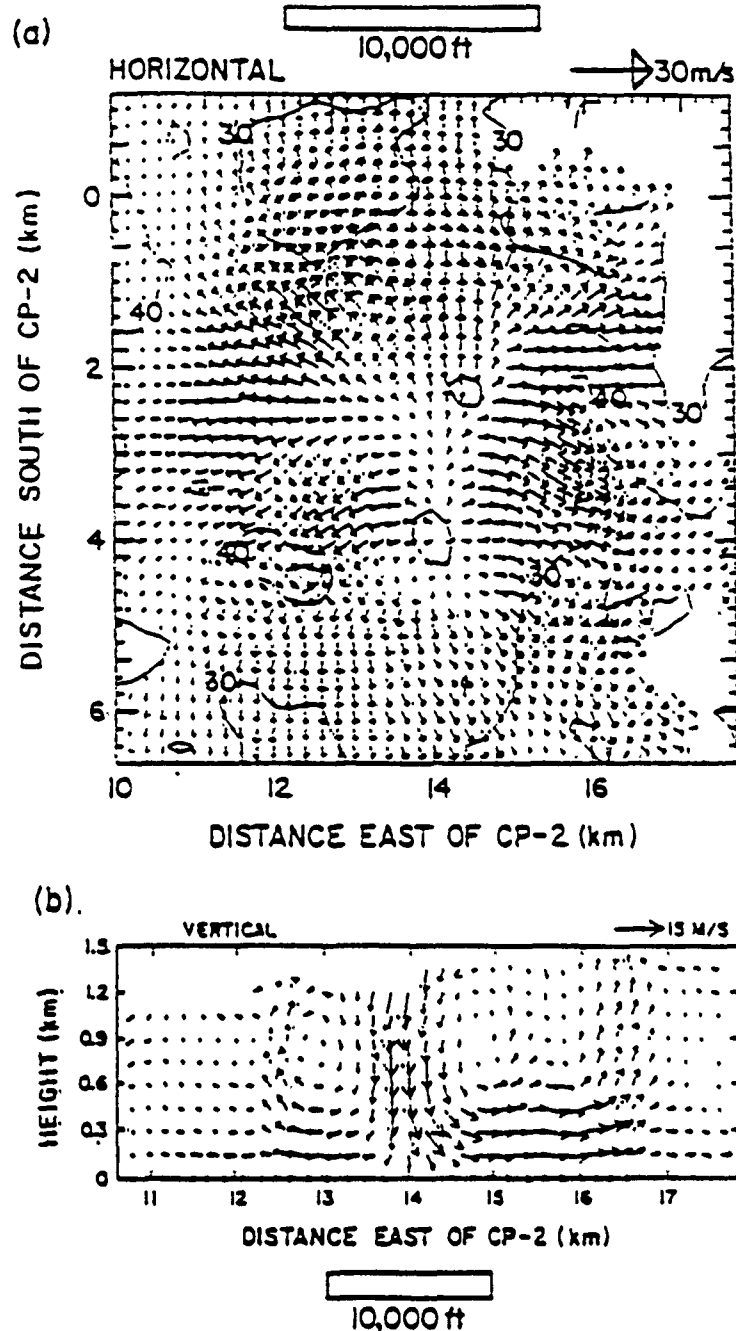
10,000 ft

Fig. 1.4 Dual-Doppler radar analysis of an intense, 14 July 1982, microburst event. Horizontal wind and reflectivity field are shown at the 0.25 km level in (a) with a vertical cross section provided in (b). A typical 10,000 ft jet runway is outlined for reference. (From Wilson et al., 1984).

12

2. STATEMENT OF THE PROBLEM

This study is designed to investigate the kinematic, dynamic and thermodynamic properties of a multiple microburst-producing storm, which occurred on 5 August 1982 in Colorado. Emphasis will be placed on horizontal grid scale refinement to obtain better resolution for data analysis. The focus will be placed on both internal and external features of microburst phenomena and its resultant interaction with/within the PBL.

Dual-Doppler radar data collected during JAWS in the summer of 1982 near Denver's Stapleton International Airport will be analyzed using a 0.25 km horizontal grid spacing. A comparison will then be made between the current study using the 0.25 km resolution and the previous study which used a 0.5 km resolution. Throughout such a comparison, the structure and internal dynamics of a multiple microburst-producing storm in the boundary layer can be further understood. Specifically, our aim is to reduce Coover's (1988) 500 m horizontal grid datum to 250 m in hopes of obtaining finer resolution for microburst structural feature investigation and recognition. A data set comparison will then be made between the two studies in order to gain better understanding and insight toward the reality of microburst phenomena as captured by Doppler radar. Doppler analysis techniques will also be further understood and an optimum horizontal grid space for use in Doppler research will be proposed.

3. AUGUST 5, 1982 MICROBURST CASE

3.1 Synoptic Weather Conditions

The synoptic scale picture for the U.S. at 0600 local standard time (LST) on 5 August 82 depicted a pair of low pressure systems; one located in southeast Montana and the other dominating the Oklahoma panhandle/southwest Kansas regions (Fig. 3.1). A quasi-stationary front extended from the Montana low through northeast Colorado into the central plains states, bisecting the mid Mississippi/Ohio valley regions and exiting the U.S. through the upper Adirondack mountain range. High pressure flanked the lows and was centered over northwestern Colorado. The front moved slowly throughout the day with the jet stream located from Oregon through Idaho, departing the U.S. from northeast Montana.

Denver's 0700 LST 5 August 1982 rawinsonde (Fig. 3.2) displayed a well mixed boundary layer extending to 1.5 km above ground level (AGL). The convective condensation level was located at 650 mb with a surface temperature of 30° C. Also, moist conditions prevailed aloft throughout the depth of 4-7 km. An average mixing ratio value of 6.5 g kg^{-1} existed within the 3 km thick moist layer. Note the lack of mid-level dry air common to most upper/high plains soundings. The height of the wet bulb (0° C) temperature is 2.8 km AGL, indicative of a hail producing storm.

The sounding exhibited conditional instability with little lift or
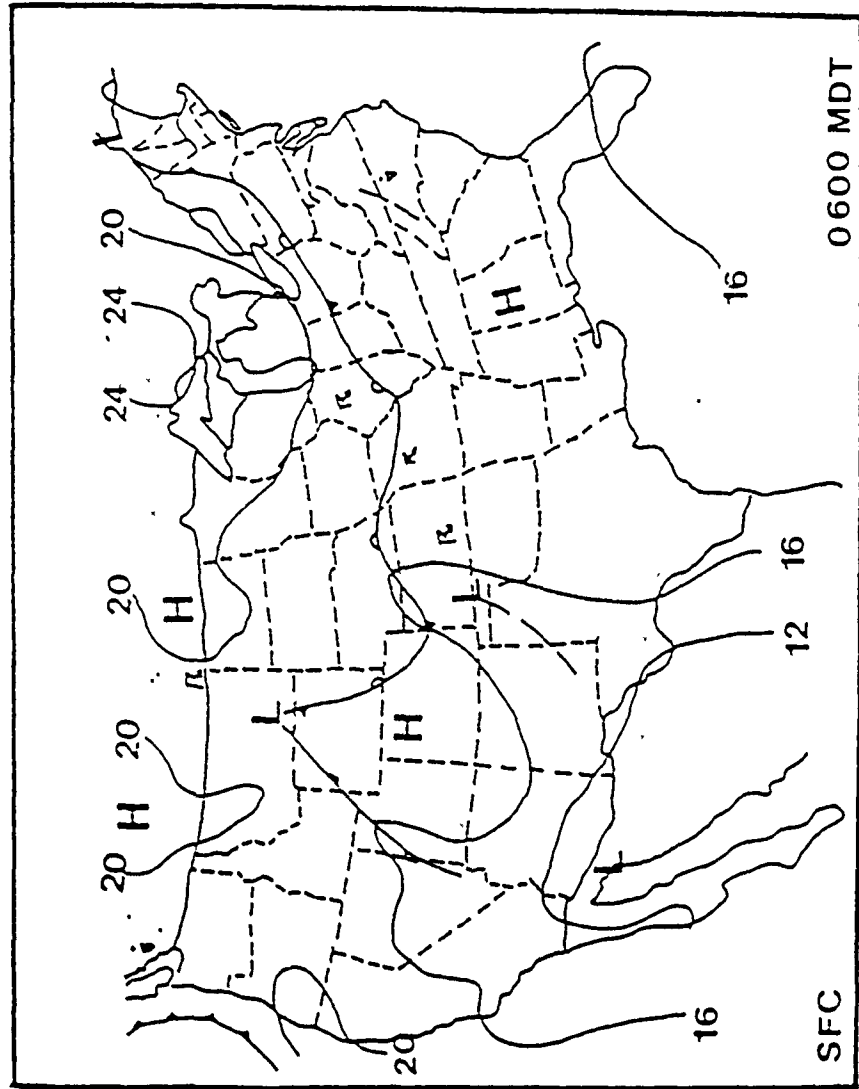
Fig. 3.1 Synoptic situation, 0600 LST, 5 August 1982.
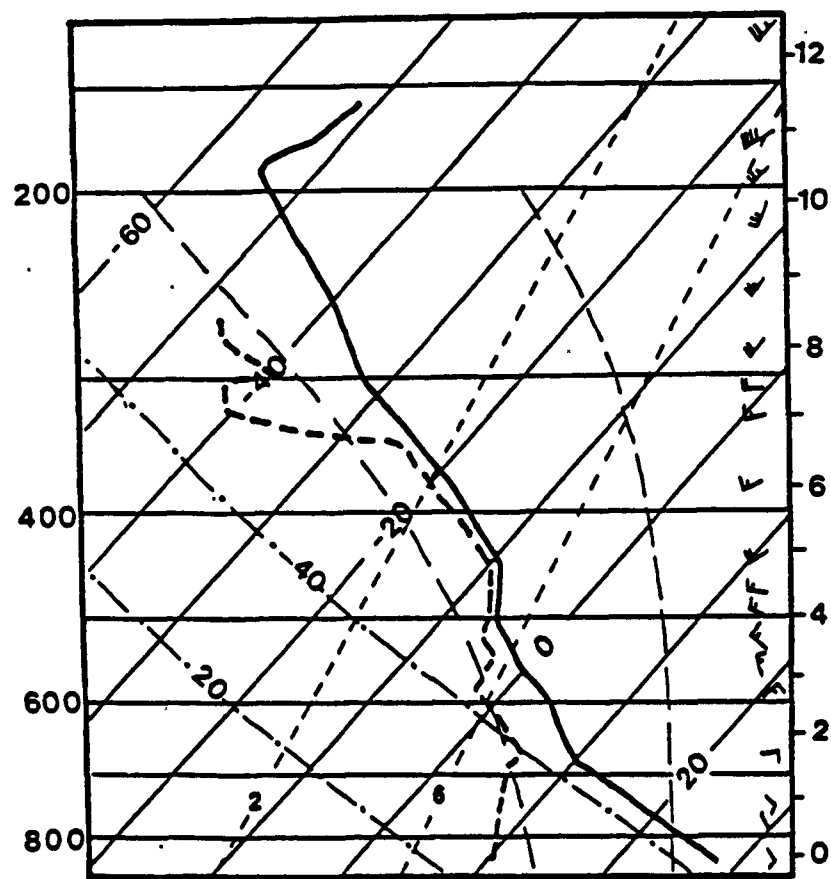
Fig. 3.2 Denvers' 0700 LST rawinsonde for 5
August 1982.

increase of surface temperature required to spark convection. Winds were observed to back sharply with height. The upper level instability (UI) was 4.0, with a 700 mb dew point of 7° C corresponding to an area too moist for downburst, but thunderstorms are still likely to develop, Caracena et al. (1983). Therefore, the dynamics which governed these microburst events may be different than other studies which based other mechanisms on microburst formation.

3.2 Data Analysis

Raw Doppler data are generally archived in unified format (UF) as noted by Barnes (1972). JAWS data were no exception with a single magnetic tape for each radar encompassing its respective data integrity for future research. Doppler data must be processed with care to minimize error and extract the physical significance of the meteorological parameter under investigation. Additionally, various consistency checks are required to assure data integrity and verify the plausability of those features observed. A complete description of the process used can be found in Pasken and Lin (1982) and Lin et al. (1986). A short discussion of the process is given below.

Hildebrand and Carbone (1980) explained that any multiple Doppler technique relies on collection of radial air velocity components in the radar's spherical coordinate system, which are then interpolated to a new coordinate system (either Cartesian or cylindrical). Calculation of horizontal velocity components (planar in the cylindrical coordinate system) follow and finally, vertical or cross planar velocities are

obtained using an imposed boundary condition (upper or lower) and the assumption of mass continuity. However, emphasis must also be placed on the wide range of uncertainties which are implicit in these data manipulations. Hildebrand and Carbone (1980) noted uncertainty and biasing in the radial velocity estimates occur as well as errors introduced during interpolation to the chosen grid. Additionally, errors in the assumed boundary condition arise and additive errors in the (cross plane) velocity estimates resulting from small errors in the horizontal divergence fields.

Pasken and Lin (1982) outlined the sequence of Saint Louis University's Doppler Radar Analysis System (SLU DRAS) below:

(1) Desired data are extracted and archived according to time and altitude.

(2) Values exceeding pre-set tolerances are eliminated, ambiguous "folded" velocities corrected and side lobe contamination deleted.

(3) Data are converted from the radar's spherical coordinate system to Cartesian coordinates.

(4) Spatial scattering of data contained in a given space are interpolated to a two-dimensional grid array.

(5) The three-dimensional wind field is computed from the gridded fields of reflectivity and two dimensional radial velocity.

(6) Thermodynamic retrieval is performed.

(7) Complete data are displayed for analysis.

3.3 Error Analysis

Based on studies by Ray et al. (1980), Doviak et al. (1980) and

Lin et al. (1986), the derived wind field is subject to both random and non-random errors. Bohne and Srivastava (1976) showed that the accuracy of the horizontal wind components for random errors, which are independent of height, to be approximately 1 m s^{-1}. Lin and Pasken (1984) indicated that other sources of error in the derived wind field are caused by advection/evolution problems, the scan rate not being compatible with the temporal evolution of the storm, errors in radial velocity estimates, due to side lobes in the antenna beam illumination patterns, incorrect upper or lower boundary conditions and biases of the radial velocity, due to ground clutter and inadequate spatial resolution to resolve relevant features in the data.

Using JAWS data sets and assuming a value of unity for radial velocity variance from dual-Doppler radars, Wilson et al. (1984) conducted error estimates for statistical uncertainty and showed that these errors combined with geometric considerations are about 1-2 m s^{-1}. Ray et al. (1978) found errors in the horizontal wind speeds to be less than 3 m s^{-1}. Doviak et al. (1976) estimated errors in wind field to be $10°$ in direction and 1 m s^{-1} in speed. Lin and Pasken (1982), Elmore (1982) and Nelson and Brown (1982) conducted error analysis on other data sets and each arrived at similiar values.

Random errors in the velocity measurements are due to statistical fluctuations associated with variance in the probability density of the assumed drop size distribution. They are compositely linked to the collection of hydrometeors within the scanned volume at the time in question, sampling techniques and pulse volume dwell times. Gal-Chen

(1982) and Chong et al. (1983) noted that uncertainties in vertical velocities are due to advection/evolution problems. Parsons et al. (1983) tested the advection correction scheme proposed by Gal-Chen (1982) to account for the temporal differences in scanning the storm volume and found that velocity errors were reduced by an order of magnitude as a result of the correction. However, when a moving coordinate system is considered, the advection error can be substantially reduced.

The assumption of the local steady state in the momentum equations will contribute errors to the retrieval of dynamic and thermodynamic variables (Hane et al., 1981). This assumption is commonly made in Doppler studies. It implies that there is no evolution within the convective system during the entire volume scan, say 2-4 min. Simulation studies by Gal-Chen (1978) and Hane et al. (1981) showed that the only way to reduce the evolution error is to scan the storm more rapidly.

Additional sources of errors which could contribute to thermodynamic retrieval include the parametric estimates of precipitation loading and friction. A sensitivity study will be conducted to determine the impact of these errors on the retrieved fields of pressure and buoyancy perturbations. We intend to conduct a detailed error analysis in order to determine the level of confidence of the derived fields.

Equipment errors include dropped bits, incorrect data processing due to low signal to noise ratio, voltage/power fluctuations within the

radar and problems similiar to those associated with the variance measurements. Non-random errors include those associated with limiting assumptions and various numerical/calculation techniques. Limiting assumptions include choice of the V_t-Z relationship employed, the adiabatic-hydrostatic atmospheric density assumption and the quasi-steady state assumption. Great effort was made to coordinate scan strategies of the JAWS Doppler radars to assure they scanned the same storm volume at the same time. The condition is believed to be met for our 5 August 1982 shallow volume scan microburst case.

The thermodynamic retrieval method of Gal-Chen (1978) is indirect and, therefore, it is necessary to check the accuracy of the retrieved fields of pressure and temperature perturbations. Gal-Chen and Hane (1981) suggested several indirect methods to verify the retrieved fields; including numerical simulations, momentum checking, and time continuity and physical plausibility. Hane et al. (1981) used numerical simulations to verify the retrived pressure and buoyancy fields using model-simulated data. Momentum checking and time continuity were employed by Gal-Chen and Kropfli (1984), Roux et al. (1984), Hane and Ray (1985) and Lin et al. (1986) to verify the retrieved fields of thermodynamic variables using real Doppler data. Momentum checking provides a relative measure of the validity of air motions as obtained from radar and a measure of how well the pressure gradients are retrieved within the domain. If the E_r value exceeds 0.5, the information retrieved contains as much noise as information. However, Hane and Ray (1985) pointed out that fields which contain much relevant information can also produce large E_r values in the

neighborhood of 1. Thus, E_r should only be considered as a relative measure of "goodness" of fit of the perturbation pressure gradients and the known functions F and G. The formula for E_r is presented in chapter 4. It is equally important to examine the physical consistency of thermodynamic perturbations with respect to the storm's kinematic structure at various times. For example, the retrieved fields must be in overall agreement with the fields of vertical velocity, convergence/divergence and vorticity. Further, the retrieved fields should maintain a time continuity from one analysis time to the other. Therefore, it is necessary to examine the consistency of the retrieved fields as well as the momentum check values to determine the level of confidence before any meaningful physical interpretation can be properly made.

4. METHODOLOGY

Doppler weather radar data was collected during JAWS from three locations within the vicinity of Denver's Stapelton International Airport. NCAR's CP-2, CP-3 and CP-4 radars formed a triangle with base lines of length 15, 18 and 28 km (see Fig. 4.1). Technical characteristics of each radar are outlined in Tables 4.1, 4.2 and 4.3. Data were collected in two minute time scans by increasing the elevation angle after each azimuth sweep. Shallow volume scans were centered on 1845, 1847 and 1850 LST on 5 August 1982. As noted by Hughes (1986), Coover (1989) and McNamee (1989), a microburst was detected at 1846 LST near the center of the analysis domain.

These shallow volume scans provided data on five vertical levels ranging from 0.25 to 1.25 km with a 0.25 km vertical resolution. Previous studies by Coover (1988) employed 0.5 km horizontal grid spacing, but this study reduced the grid spacing to 0.25 km in hope of obtaining finer resolution of the 1845 LST 5 August 1982 microburst event. Data obtained via Doppler radar is collected in radial (along the beam axis) form and must be judiciously edited prior to transformation to a Cartesian coordinate system for further manipulation.

4.1 Reduction of Initial Data Field

Extracted data consist of azimuth sweeps subtending approximately a 90° of arc. Data falling outside the domain of interest was deleted by extracting only the rays within a specified range of angles.
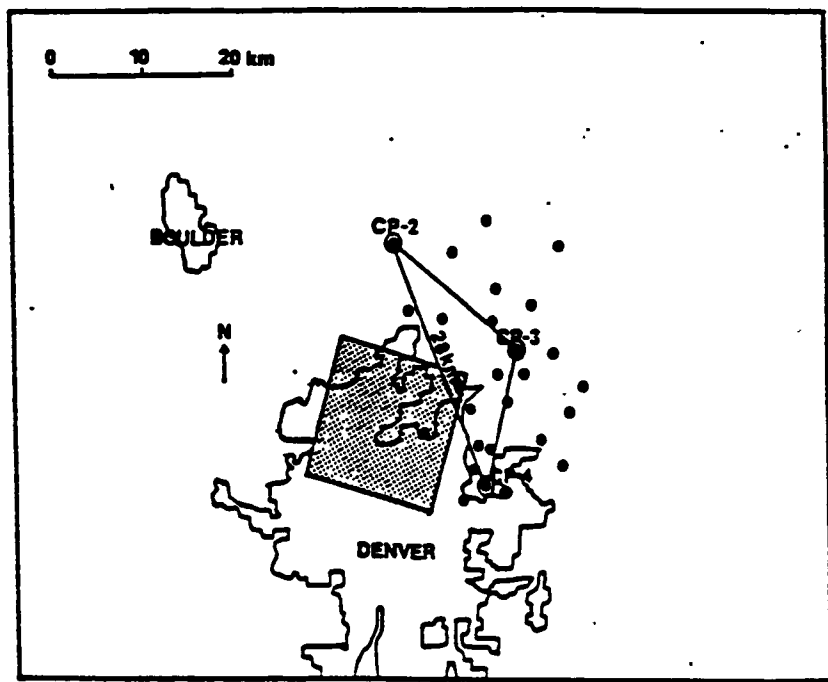
Fig. 4.1 Geometric stratagem between Doppler radars and the JAWS territorial domain.

Table 4.1

Radar locations in latitude, longitude and CP-4 relative coordinates

Radar	Latitude (deg min sec)			Longitude (deg min sec)			Elev (m)	CP -2 Coordinates (km) X	Y
CP-2	39	59	37	104	59	39	1602*	-10.45	25.45
CP-3	39	53	34	104	49	41	1570*	14.15	-11.19
CP-4	39	45	53	104	52	19	1619*	0	0

*Height to center of beam.

Table 4.2

NCAR Doppler radar characteristics for JAWS

Parameter	CP-2	CP-3	CP-4
Wavelength (cm)	10.67	5.45	5.49
Pulse duration (us)	0.4 to 1.5	1.0	1.0
Avg. power* (dBm)	59	55	55
Pulse repetition frequency (Hz)	960 & 480	1666 & 1250	1666 & 1250
Antenna diameter (m)	8.534	3.658	3.658
System gain (dB)	43.9	43.0**	41.0***
Beamwidth (deg)	0.97	1.17	1.09
Minimum detectable signal at 10 km (dBz)*			
Reflectivity:	-25	-10	-24
Velocity:	-25	-23	-24

* Representative values
** Radar dome off
*** RAdar dome on

Table 4.3

Radar system parameters for data acquisition during JAWS

Parameter	CP-2	CP-3	CP-4
No. of samples in estimate	32, 64,..., 2048	32, 64,..., 2048	32, 64,..., 2048
No. range gates	256, 512, 768, 1024	512	512
Azimuth scan rate (deg/sec)	0-15	0-35	0-35
Min. elev. angle increment (deg)	0.1	0.1	0.2
Range gate spacing (m)	90-600	150-240	150-240
Max. unambiguous range (km)	150 & 300	90 & 120	90 & 120
Max. unambiguous velocity (m/s)	±25.7 & ±12.8	±22.6 & ±17.0	±22.8 & ±17.2

27

The data were then converted from spherical coordinates, relative to the source radar, to orthogonal coordinates, relative to one radar (CP-4). The data was edited using a velocity threshold, based on the Doppler wave propagation theory, and threshold values based on a function of the returned signal. Resultant data then sliced into slabs centered on the vertical level of interest and then horizontally interpolated to grid points via Barnes' (1973) scheme. Finally, data points are vertically interpolated to a specified horizontal plane.

Conversion from the radial velocities collected by the two radars (V_{r1}, V_{r2}) into the u,v and w components of the three-dimensional wind requires an independant measure of the terminal velocity. Martens (1975) empirical terminal fall velocity-radar reflectivity (V_t - Z) relationship for a high plains storm with the density-height correction proposed by Foot and Du Toit (1969);

$$V_t = -5.70 \ Z^{0.04} \ (\frac{\rho_{oo}}{\rho_o})^{0.4} \tag{4.1}$$

was used for the particle terminal velocity in this study where ρ_{oo} is the standard surface air density and ρ_o the actual environmental air density.

Following the studies by Armijo (1969), Brandes (1977,1978), Lin and Pasken (1982, 1984), Lin et al. (1986) and Lin and Coover (1988), the horizontal wind components (u, v) are determined from Eq. (4.1), the radial velocities (V_{r1}, V_{r2}) and Cartesion wind components (u, v, w) with respect to radial position (R_1, R_2). These values are both a func-

tion of (x, y, z) from each radar and are given by:

$$u = \frac{R_1 V_{r1}(y - y_2) - R_2 V_{r2}(y - y_1) - [(y_1 - y_2)(w + V_t)z]}{(x - x_1)(y - y_2) - (x - x_2)(y - y_1)} \qquad (4.2)$$

$$v = \frac{R_1 V_{r1}(x - x_2) - R_2 V_{r2}(x - x_1) - [(x_1 - x_2)(w + V_t)z]}{(y - y_1)(x - x_2) - (y - y_2)(x - x_1)} \qquad (4.3)$$

Finally, the anelastic continuity equation, i.e.,

$$\frac{\partial [\rho_{oa}(z)w]}{\partial z} = -\rho_{oa}(z) \vec{\nabla}_h \cdot \vec{\nabla} \qquad (4.4)$$

allows the vertical wind component, w, to be calculated where ρ_{oa} is the adiabatic-hydrostatic atmospheric density as a function of height and is approximately equal to the environmental density ρ_o as noted by Brandes (1984) and Lin et al. (1986). Equations (4.1-4.4) form a complete set of equations which may be solved for the three-dimensional wind field if the boundary value of w is known. Using the surface boundary constraint of $w = 0$, the anelastic continuity equation gives:

$$w(up) = \frac{\bar{\rho}_{oa}(lwr)(z)}{\bar{\rho}_{oa}(up)(z)} w(lwr) - \frac{\rho(avg)(z)}{\rho_{oa}(up)(z)} (\vec{\nabla}_2 \cdot \vec{\nabla}_H) \Delta z \qquad (4.5)$$

where w (lwr) is the vertical velocity at the lower level, $\rho_{oa(up)}$ is the basic density at the upper level, $\bar{\rho}_{avg}$ is the mean density averaged between two levels and $\vec{\nabla}_2 \cdot (\vec{\nabla}_H) \Delta z$ represents the horizontal divergence averaged vertically between two levels. Since the depth of the analysis domain is shallow (1.25 km), the accumulation of error during upward integration is negligible (Lin et al. 1986).

4.2 Thermodynamic Retrieval

The thermodynamic retrieval technique of Gal-Chen (1978) recovers fields of perturbation pressure and temperature from the detailed wind field using the three momentum equations. The data are obtained from their horizontal area means. The momentum equations in a moving coordinate system may be written as (e.g., Parsons et al., 1987):

$$\frac{\partial \pi}{\partial x} = -\frac{1}{c_p \theta_{vo}} \left(\frac{Du}{Dt} + f_1 \right) = F \tag{4.6}$$

$$\frac{\partial \pi}{\partial y} = -\frac{1}{c_p \theta_{vo}} \left(\frac{Dv}{Dt} + f_2 \right) = G \tag{4.7}$$

$$\frac{\partial \pi}{\partial z} = -\frac{1}{c_p \theta_{vo}} \left(\frac{Dw}{Dt} - g\beta' + f_3 \right) = H \tag{4.8}$$

where Du/Dt, Dv/Dt and Dw/Dt are accelerations along the x-, y-, and z-axes respectively; f_i (i = 1, 2, 3) forces other than pressure gradients; $\pi = (P'/P_{\infty})^{R/c_p}$ a perturbation Exner function; θ_{vo} the mean virtual potential temperature, R the specific gas constant and c_p the specific heat at constant pressure. The buoyancy parameter, β', is approximated as:

$$\beta' = \frac{\theta'}{\theta_o} + 0.61 q'_v - q_l \tag{4.9}$$

where the subscript o and prime denote the mean and the deviation from that mean, respectively; q_v the water vapor mixing ratio and q_l the condensate mixing ratio.

The horizontal nondimensional perturbation-pressure equation at a given level can be derived from (4.6) and (4.7) to yield

$$\frac{\partial^2 \pi}{\partial x^2} + \frac{\partial^2 \pi}{\partial y^2} = \frac{\partial F}{\partial x} + \frac{\partial G}{\partial y} \qquad (4.10)$$

Equation (4.10) is solved by successive overrelaxation with the Neumann boundary condition imposed. The unique solution of (4.10) exists only if the horizontal average is removed from each horizontal plane of π in (4.10). The pressure deviation, P'_d, can then be determined from the nondimensional quantity using the relationship $P'_d = P_{oo} \pi^{c_p/R}$.

As discussed earlier, momentum checking provides a measure of the validity of the retrieved data and is indicated by E_r. The relative error in pressure retrieval is given by the formula:

$$E_r = \frac{\iint [(\frac{\partial \pi}{\partial x} - F)^2 + \frac{\partial \pi}{\partial y} - G)^2] \, dxdy}{\iint (F^2 + G^2) \, dxdy} \qquad (4.11)$$

Once the field of π is obtained, the deviation-perturbation virtual potential temperature field, θ'_{vd}, can be calculated from the buoyancy equation, i.e.,

$$\theta_{vd}' = \frac{\theta_{vo}}{g} \underbrace{(c_p \theta_{vo} \frac{\partial \pi}{\partial z}}_{VPG} + \underbrace{(\frac{Dw}{Dt} - <\frac{Dw}{Dt}>)}_{VAC} + \underbrace{g(q_r - <q_r>)}_{RWL} + \underbrace{(f_3 - <f_3>))}_{VFF} \qquad (4.12)$$

where terms VPG, VAC, RWL and VFF represent the contributions of vertical perturbation-pressure gradient, vertical acceleration, rainwater loading, and friction, respectively, to θ'_{vd}, and $<\ >$ denotes the horizontal area mean. With the aid of the perturbed potential temperature equation, we obtain $T'_{vd}/T_{vo} \simeq \theta_{vd}'/\theta_{vo}$. This approximation is justified since the P'_d / P_o term is much smaller than the other two

terms. The retrieved temperature represents a virtual cloud temperature since it accounts for both deviation of virtual temperature perturbation and cloudwater content (Roux et al., 1984).

5. DISCUSSION OF RESULTS

The focus of this study is the meteorological interactions with and within the PBL associated with microburst and LLWS phenomena. Data captured by the JAWS include the radial velocity components (along beam axis), reflectivity patterns and altitude data for each individual scan. The three-dimensional wind velocities, perturbation pressure and temperature fields were calculated using this data. The results from this study show that intense small scale downdrafts like microburst events are characterized by perturbation pressure gradients which act as an accelerating force, driving the phenomena throughout its evolution. This is in agreement with previous research by Lin et al. (1987), Lin and Hughes (1987) and Lin and Condray (1987).

Dual-Doppler analysis studies similar to this one allow the cascade of energy from observable to high wave number smaller scales to become more readily understood. The case studies presented depict separate microburst events within the domain of interest. Coover's (1988) previous study used 500 m horizontal grid spacing for the 1845 LST 5 August 1982 microburst case. This study employs a 250 m horizontal grid datum obtaining a finer resolution of the kinematic, dynamic and thermodynamic features of the 1845 LST microburst analysis period. Through case study and data set comparison, those structural features associated with microburst are made more apparent. An optimum horizontal grid datum for dual-Doppler analysis will also be proposed.

33

Analyses are presented below by disecting each horizontal level of interest (0.25 thru 1.25 km) for structural features. Data provided are for both the 500 m horizontal grid space domain from the previous study, and for the 250 m horizontal datum employed in the current study.

5.1 Plan View: 250 m Grid Scale Analysis

A Barnes objective analysis conducted with a 250 m horizontal grid spacing was performed· with a 0.875 km scan radius. The smaller grid domain should provide finer resolution of those events captured during the 1845 LST period by dual-Doppler radars during the JAWS project. Analyses are conducted by disecting five horizontal levels separated at 250 m intervals for the structural features of those storms present. Storm features resolved at the 500 m grid scale analysis are significantly more pronounced at the smaller grid domain and will be disscussed later. Additional features of interest also become apparent at the smaller grid scale. Data fields of reflectivity, vertical velocity along with perturbation pressure and temperture are presented below with distances in kilometers relative to the CP-4 radar.

Figure 5.1 displays the plain view of the 0.25 km level horizontal wind and reflectivity field using 250 m horizontal grid spacing. Similar to the 500 m horizontal grid spacing analysis, two microburst events are visible (M1 and M2) and found to be situated near or within the areas of highest reflectivity (values of 50 dBZ or greater). The dominant microburst feature, M1, is located at x=-11.5 and y=1.5 km.
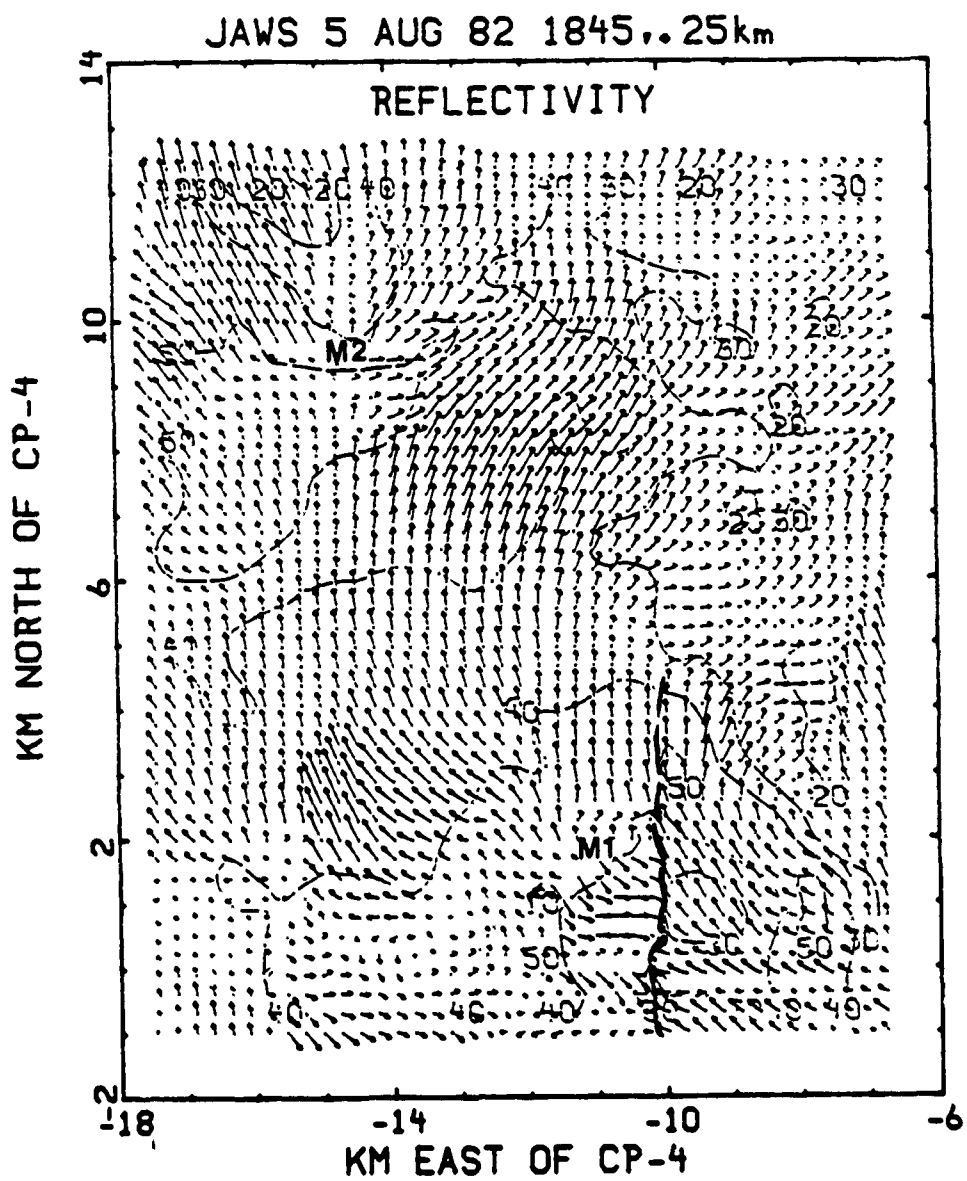
Fig. 5.1 Plan view: Horizontal wind and reflectivity field for 5 August 1982, 1845 LST case using 250 m horizontal grid spacing at 0.25 km.

Microburst M2 is located northwest of M1 near x=-14.5 and y=9 km. The second microburst, M2, is strikingly more visible than it was in the 500 m grid analysis. The environmental flow at this level is from 220° at 6-8 knots. A gust front is noted at the southeast portion of the grid, indicated by the dashed line, and results from M1's eastward divergent outflow boundary and the cyclonic circulation (inflow) just south of the shear line. An additional cyclonic circulation is found to appear to the west southwest of M1 (-15.5,1.0), a feature which goes unnoticed at the larger grid spacing. The maximum divergence associated with M2 is displaced downwind of its highest reflectivity core and largely due to a coupling between the environmental wind and strength of the M1 outflow boundary.

The temperature field for this level (Fig. 5.2) reveals cold values of -3°C and -2°C associated with M1 and M2's position, respectively. Perturbation temperature values of -1°C accompany the gust front region to the east of M1 and the cyclonic circulation in the southwest portion of the grid. Both microburst events have cold cores and are separate entities, although M2's cold core and divergent structure are clouded by M1's strong outflow and the environmental mean wind. All features are flanked by warm temperatures with values between 1°C and 2°C, indicative of initial updraft regions. A warm anomaly (2°C) located in the central portion of the grid may be due in part to surrounding terrain features and partially due to the one sided finite differencing scheme employed at the lowest level. A net decrease of 200 m between the microburst location and the anomaly location result in a channeling and acceleration of flow. Therefore, strong downslope
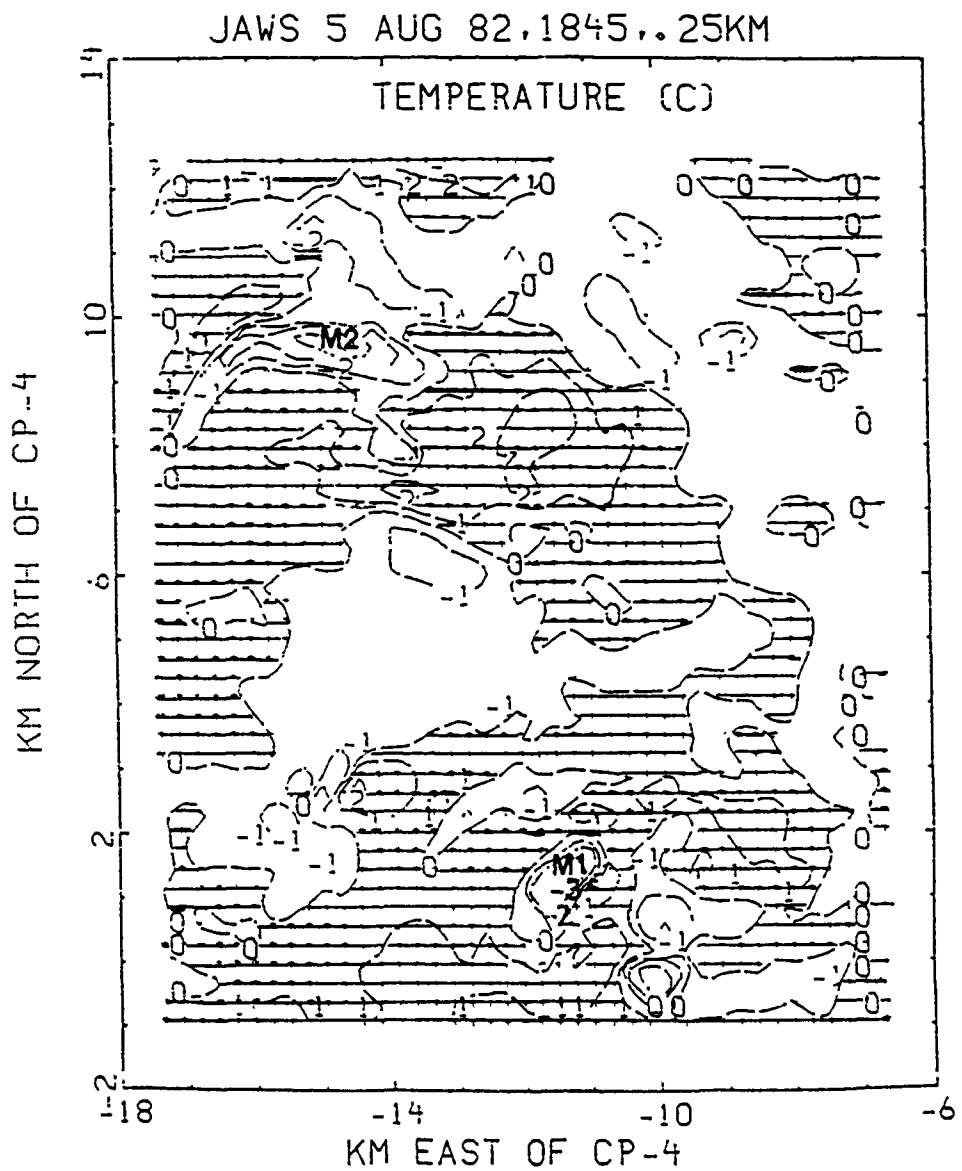
Fig. 5.2 Perturbation temperature field for the 5 August 1982, 1845 LST case using 250 m horizontal grid spacing at 0.25 km.

winds are at least partially responsible for the central grid region warm anomaly. The pressure field for this level (Fig. 5.3) indicates high pressure regions (20 Pa/0.2 mb) accompany each microburst event. Low pressure anomalies correspond to updraft areas and a value of -30 Pa (-0.3 mb) is noted for the cyclonic circulation in the southwest grid area, due west of M1. Vertical velocities of -1 to -2 m s^{-1} accompany M1 and M2 with updraft strengths of 2-4 m s^{-1} surrounding each event.

The 0.5 km level (Fig. 5.4) depicts both microburst areas as active, though slightly less pronounced than at the lower level. The microbursts are still centered in core of the high reflectivity regions. Both cyclonic circulations within the vicinity of M1, one associated with the surface gust front to its east and the other due west in the southeastern portion of the grid, remain present and well defined. However, the gust front has shifted its position approximately 1 km to the west-northwest with its parent cyclone still intact at the base of the grid. The vertical velocity field for this level (Fig. 5.5) indicates values of -3 and -1 m s^{-1} for microbursts M1 and M2, respectively. The maximum divergence associated with M2 continues to be shifted to the downwind side. The vertical velocity profile clearly identifies M1 and M2 as areas of sinking motion. A ring of upward motion flanks both microburst events. Updraft speeds vary from 1 to 2 m s^{-1} and correspond to microbursts M1 and M2 accordingly. The cyclonic circulation due west of M1 in the southwest grid region carries a downdraft value of -1 m s^{-1} with a corresponding updraft of 1 m s^{-1} to its northeast. The vertical velocity field thus provides credence for all
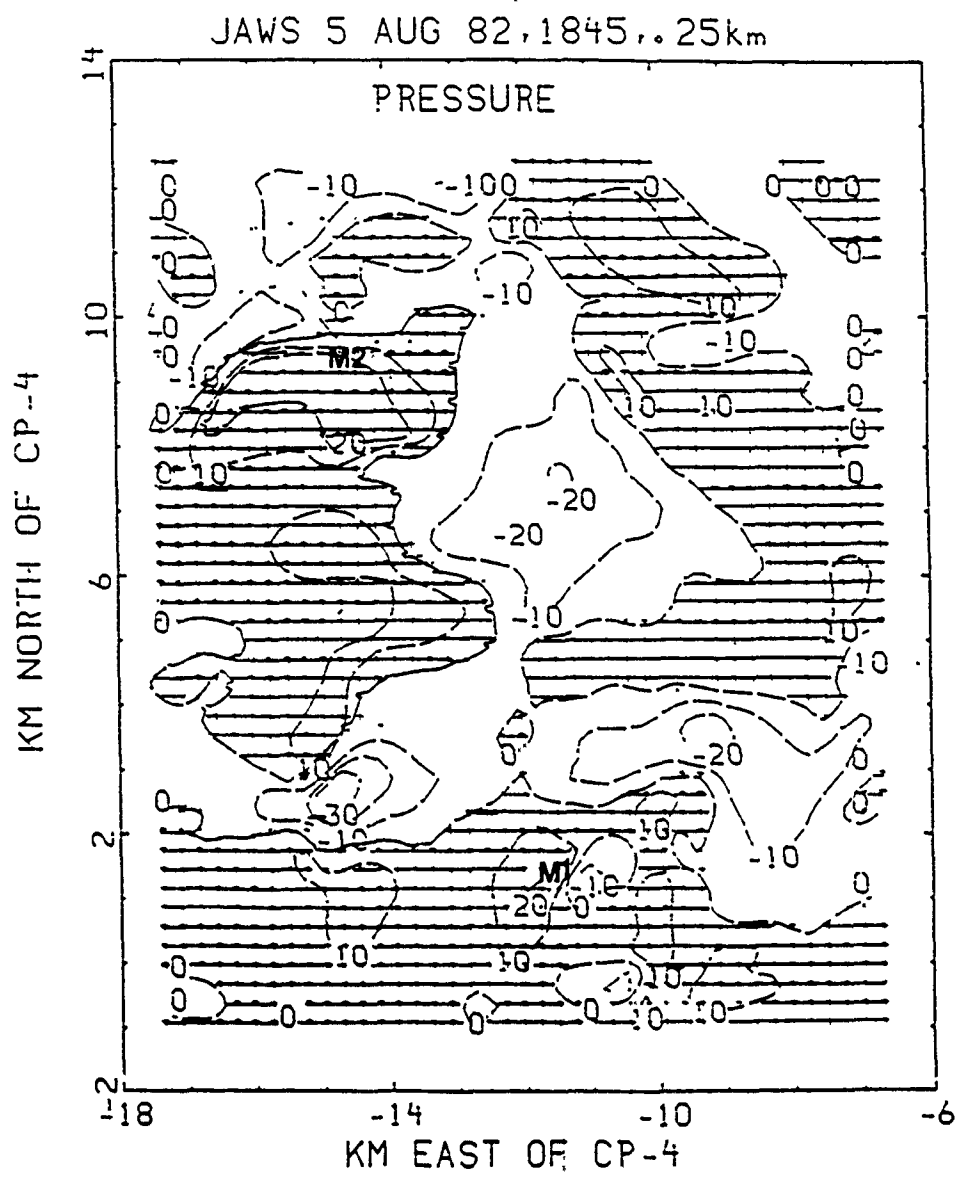
Fig. 5.3 Perturbation pressure field for the 5 August 1982, 1845 LST case using 250 m horizontal grid spacing at 0.25 km. Units are in Pascals where 10 Pa equals 0.1 mb. To convert units to mb, multiply by a factor 0.01.

JAWS 5 AUG 82 1845,.50km

REFLECTIVITY
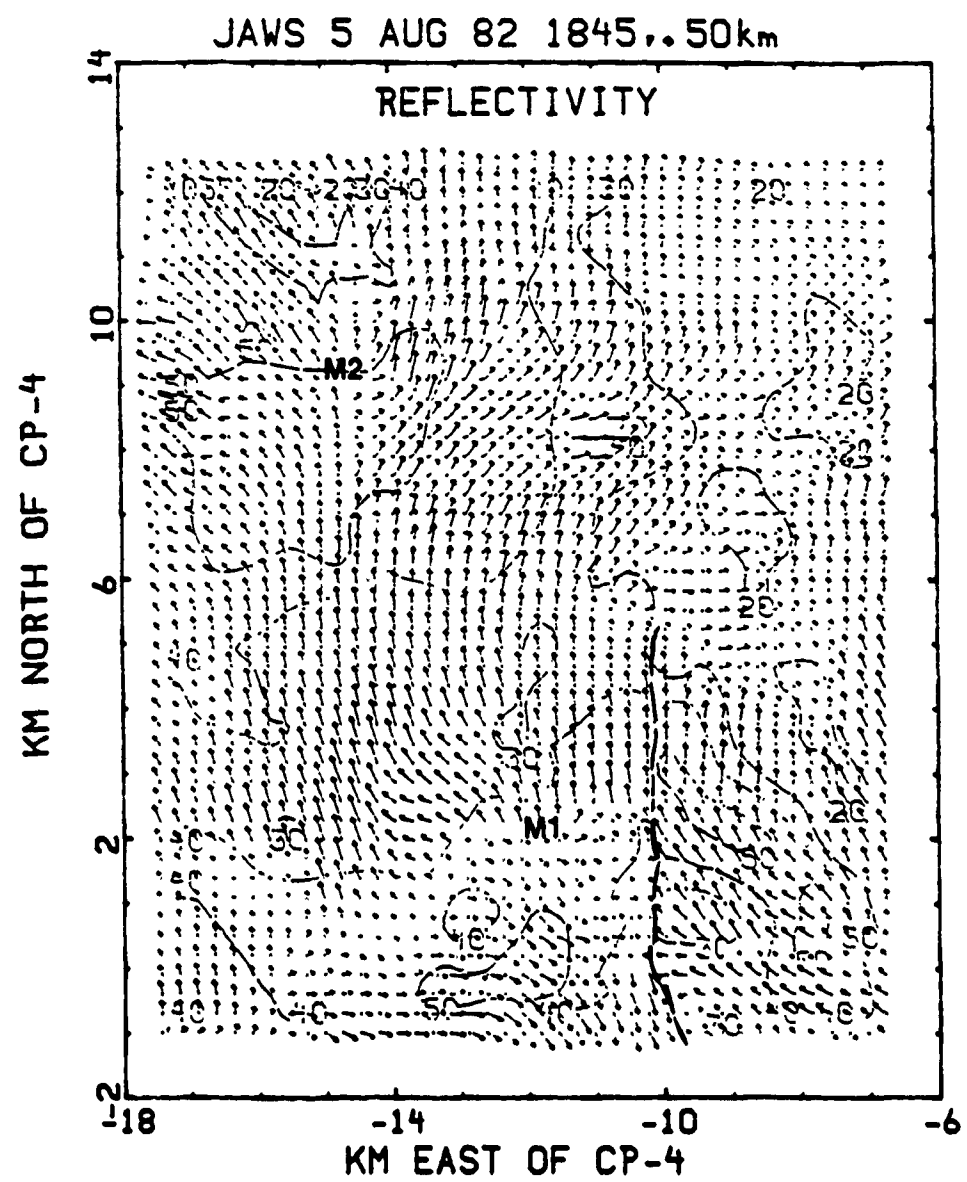
Fig. 5.4 Same as Fig. 5.1, except for 0.50 km.
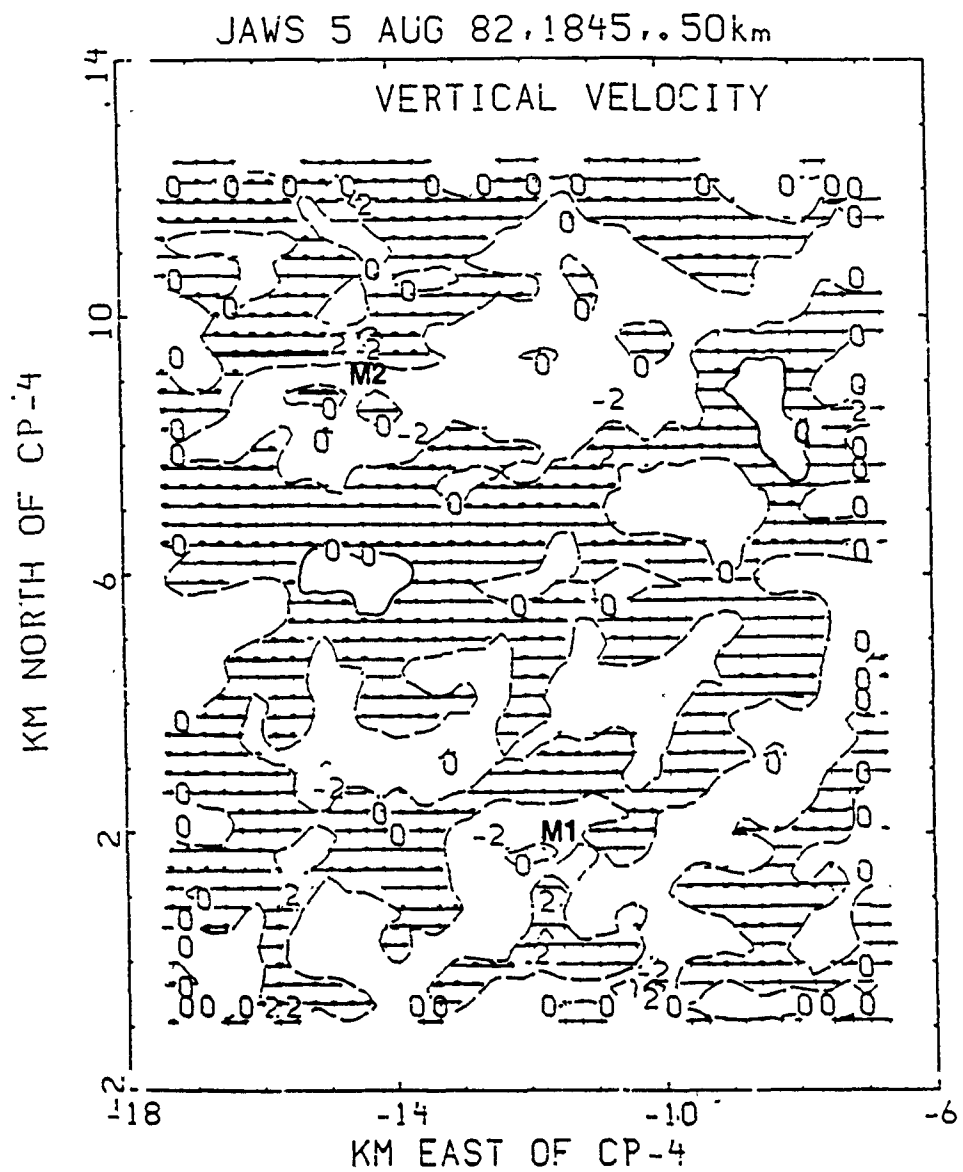
Fig. 5.5 Vertical velocity profile for the 5 August 1982, 1845 LST case using 250 m horizontal grid spacing at 0.50 km.

features presented. Upon examining those parameters discovered thus far, we found that a good correlation should exist between the vertical velocity and pressure fields.

The perturbation pressure pattern for the 0.5 km level (Fig. 5.6) shows each microburst event to be a high pressure anomaly. Maximum values are 20 Pa (0.2 mb) for both M1 and M2. Low pressure may be found along the gust front and generally surrounds the microburst high pressure regions thus supporting convergent updraft areas surrounding each event. The cyclonic circulation due west of M1 is also found to be a slight low pressure anomaly. The temperature field at 0.5 km (Fig. 5.7) is less clear but still indicates that each microburst is typified by a cold core anomaly. Each microburst has a temperature deficit of about -1°C, while a warm pool of air (2-3°C) exists near the center of the grid domain. This temperature pattern is consistent with the 0.25 km level. Areas of strong updrafts are associated with convergence between terrain induced features, the environmental flow and M1's strong outflow boundary discussed earlier. The cyclonic circulation near the gust front still has a temperature deficit associated with it. The deficit is larger than at 0.25 km as upward vertical motion increases; thereby, cooling the unsaturated inflow air by dry adiabatic expansion. A cool temperature perturbation of -2°C corresponds to the gust front cyclone, while a value of -1°C accompanies the cyclone in the southwest of the grid, indicative of dry adiabatic expansion associated with its 1 m s^{-1} northeast flanking updraft. A significant point is the 1 km shift to the west northwest of M1's central core.

PRESSURE
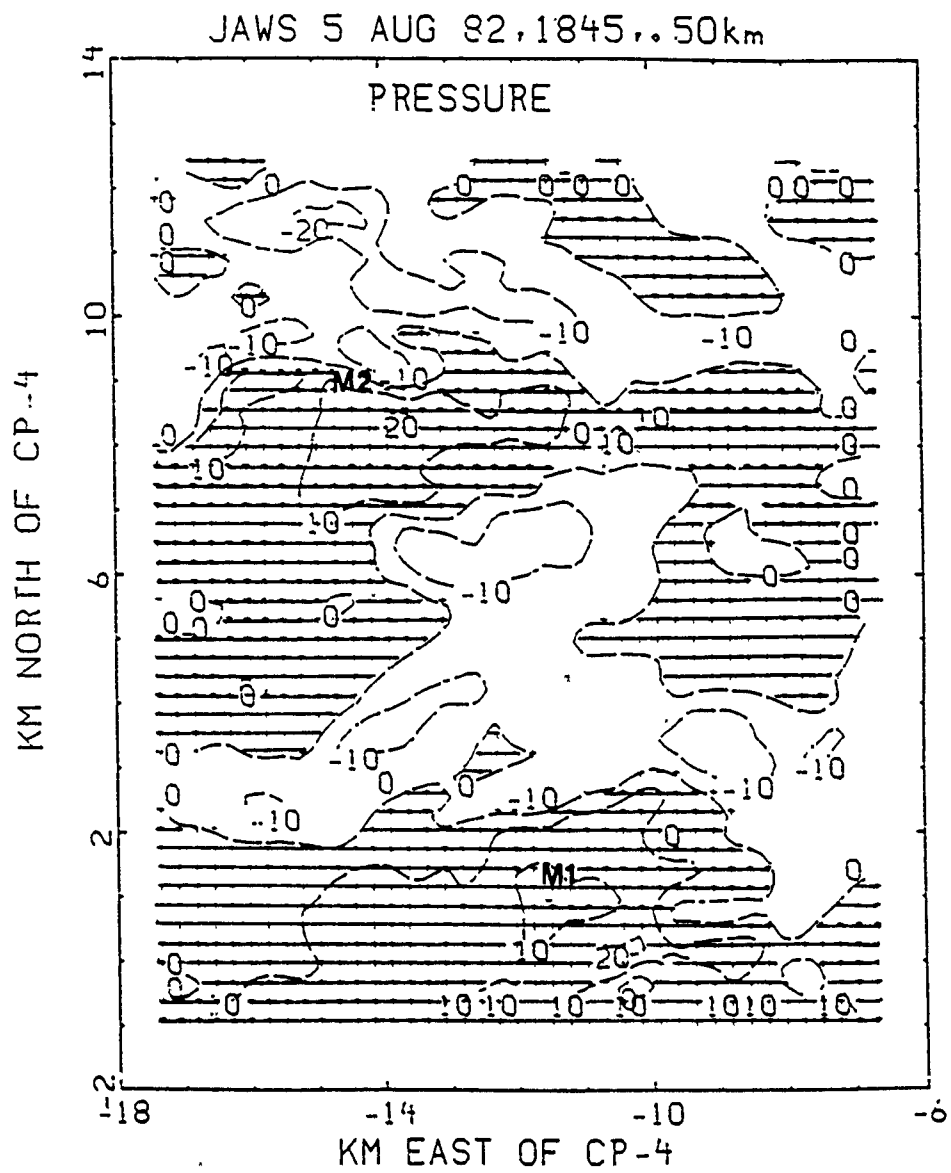
Fig. 5.6   Same as Fig. 5.3, except for 0.50 km.
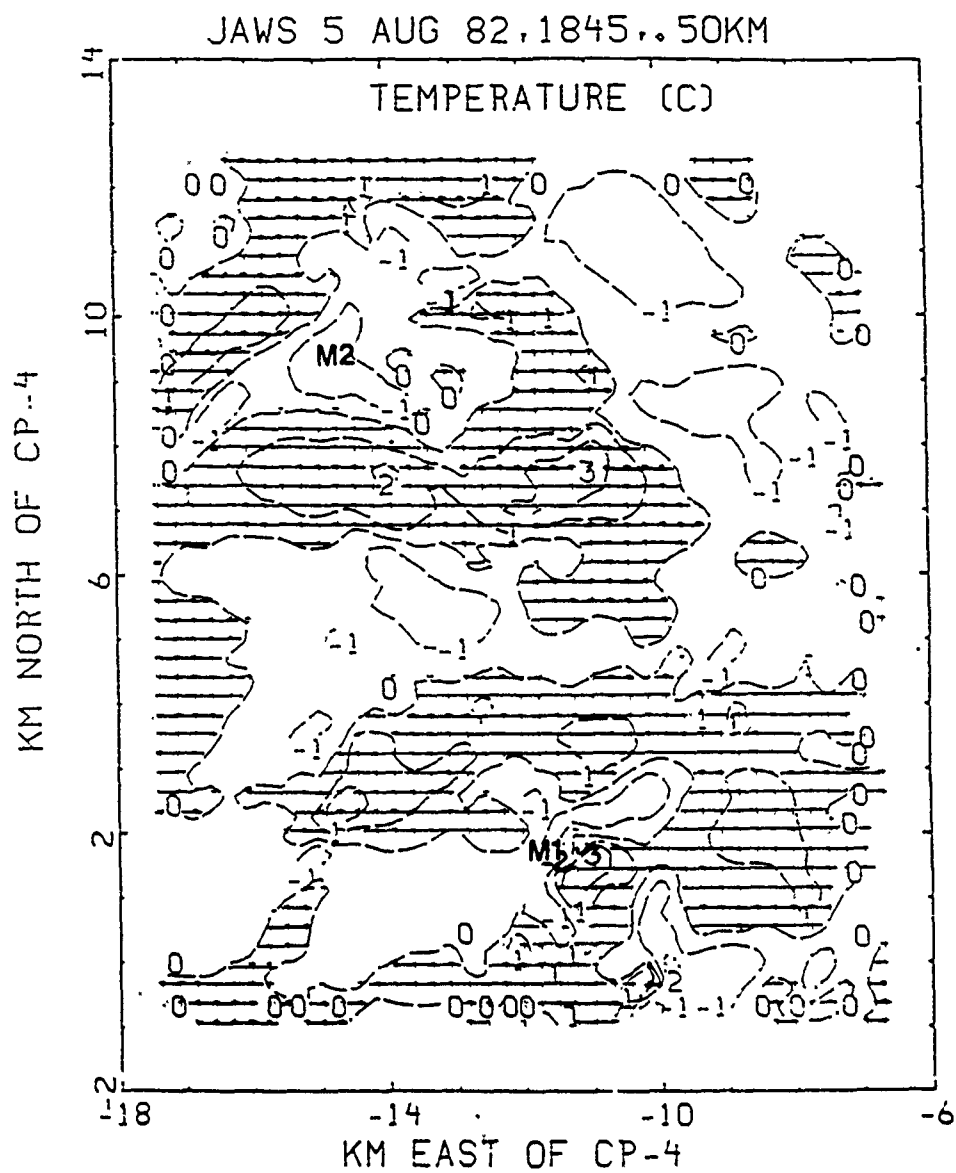
Fig. 5.7   Same as Fig. 5.2, except for 0.50 km.

Structural features are seen to undergo a transition at the 0.75 km level as shown by the horizontal wind field (Fig. 5.8). The environmental flow is dominant at this level. The entire wind field for the grid is predominately southeast or southerly with little horizontal eddy motion. The environmental flow actually begins to dominate the microburst core regions that persist in the 50 dBZ contour. None-the-less, the M2 outflow boundary becomes replaced by cyclonic motion. Structural changes associated with M1 are less pronounced, although cyclonic turning of the wind becomes apparent to its north. The gust front is not well defined at this level, but the cyclonic gyration to the south of its presumed position remains. The cyclonic circulation due west of M1 has completely vanished being over run by the environmental flow. Thus, it appears this cyclonic circulation extends only to 0.75 km in depth. Each microburst remains in tact with respect to vertical velocities and carry values of -4 m s^{-1}. The vertical motion at the southwest portion of the grid associated with the cyclone discovered at lower levels maintains values of -2 and 2 m s^{-1} with respect to its down/updraft areas, respectively. Even though the well defined cyclonic motion is masked at this level, apparently mass is effectively being channelled both upward and downward. Therefore, vertical velocity continues to verify the presence of the microbursts. It becomes clear that this level is one of transitional change of storm composition. The microburst downdraft does not decelerate greatly due to the effect of the earth surface, nor is it at a level where mass originates for downward transport since little entrainment occurs into the level nor transport out of the downdraft. The level thus is an active channel where mass collected from above passes down through the layer to levels

JAWS 5 AUG 82 1845 ,.75km
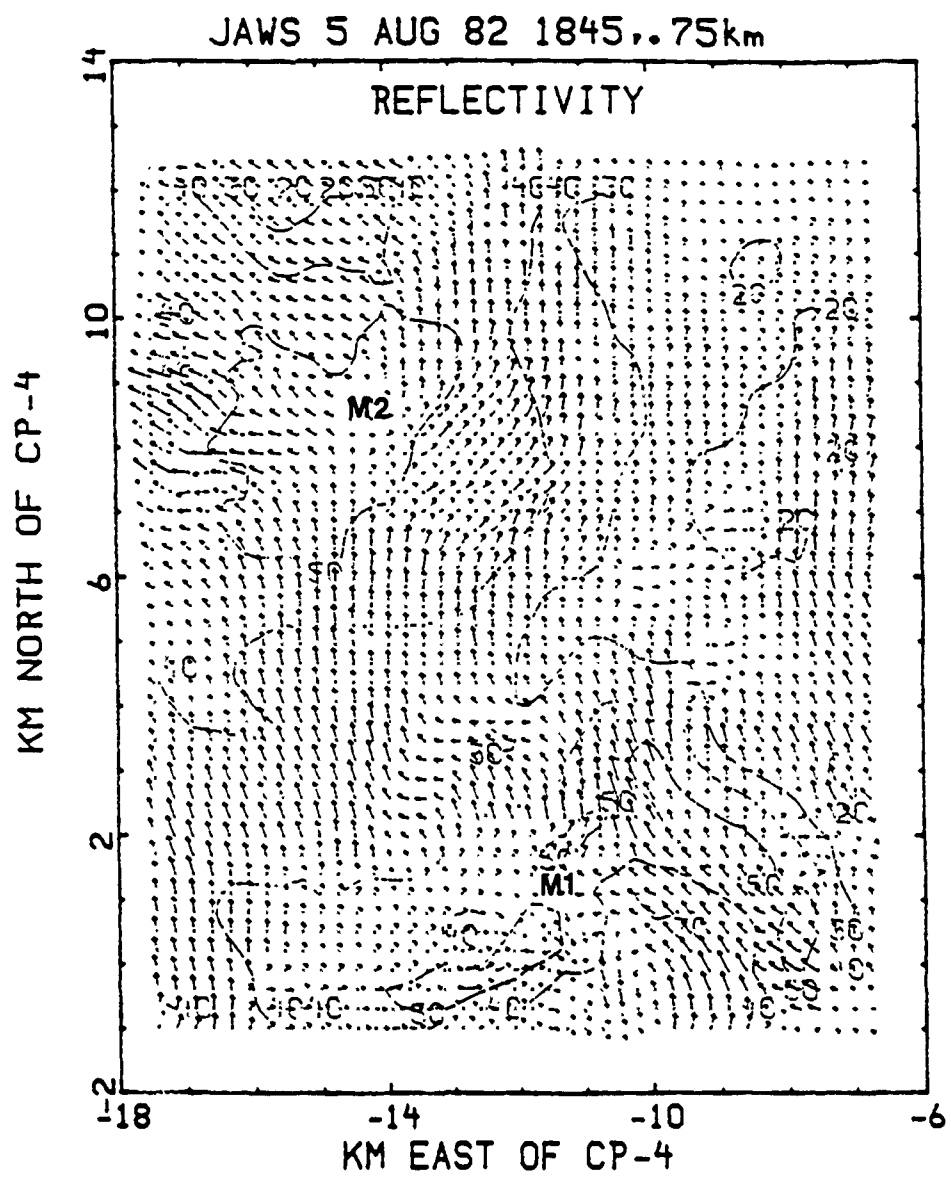
REFLECTIVITY

Fig. 5.8   Same as Fig. 5.1, except for 0.75 km.

below where it may be distributed by horizontal divergence.

The winds at this level are seen to blow parallel to the reflectivity contours to the northeast of M2 and to the southeast of the cyclonic circulation. Indications are that strong outflow of precipitation cooled air from the high reflectivity core, which occurred at lower levels, is not taking place. Entrainment of dry environmental air from flow towards higher reflectivity values is likewise absent. Therefore, dry air entrainment of environmental air should be occurring at upper levels.

Examination of the 1 km level indicates definite changes have taken place as opposed to the lower levels. The only feature which remains unchanged is the cyclonic circulation south of the presumed surface gust front location (Fig. 5.9). Otherwise, strong cyclonic motion occurs for both microbursts to the north of their central core regions. Additionally, the strong winds associated with the central grid updrafts found at lower levels are much weaker. Dry air entrainment begins to occur at the 1 km, thereby feeding the microburst events. This is evident by an increase in the crossing angle flow of the environmental air from low to high reflectivity cores, associated with the descending precipitation shaft. Additionally, cyclonic curvature becomes established on the north sides of M1 and M2. Vivid finger like protrusions in the reflectivity accompany each microburst event. A finger like appendage is noted in the reflectivity pocket southwest of M1, an area of 50 dBz, which curls counter-clockwise up the grid and back towards M1. Another finger like projection extends down the grid from the extreme northwest corner of the grid, pointing at M2. I
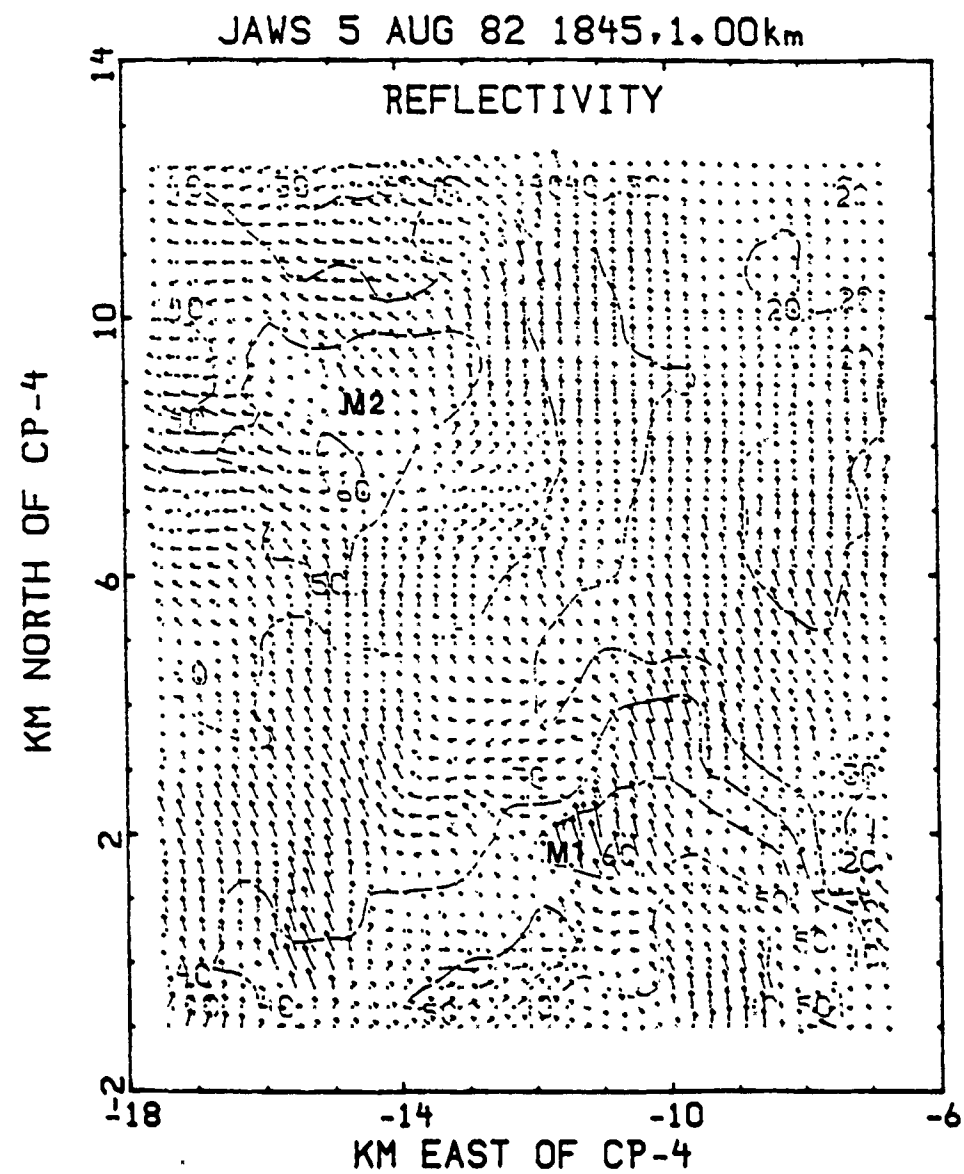
Fig. 5.9 Same as Fig. 5.1, except for 1.0 km.

refer to these finger like appendages as circulation feeders which provide abundant tongues of dry environmental air for digestion into microburst core regions. Cyclonic flow around both microburst events are much broader and more pronounced than at lower levels. The cyclonic circulation to the west southwest of M1, found absent at the 0.75 km level, begins to re-established itself at this analysis level. The streamline analysis shows a confluent asymptote connecting the low pressure microburst regions; which is fed and driven by anti-cyclonic curvature in the central portion of the grid and just northwest of M1. Anti-cyclonic flow is also visible in the southeast portion of the grid domain. Analysis at the 1.25 km level will clarify these features and provide insight toward complete microburst evolution.

Analysis of our highest storm level (1.25 km) readily identifies the two microburst events, each with a characteristic strong cyclonic circulation (Fig. 5.10). The finger like appendages discussed earlier are more numerous and tongue like in resemblance. The finger like appendages associated with the dry air intrusions are broader than 1 km and the crossing angle of environmental air toward the high reflectivity cores increase to almost perpendicular angles. Cyclonic turning of the wind occurs around both microbursts with pronounced cyclonic circulation visible around M1. Mass is thus noted to spiral inward prior to its descent within the microburst core. Cyclonic circulation again becomes apparent to the west southwest of M1 corresponding to the cyclonic gyre at this location found in the lower levels excluding the 0.75 km level. Therefore, it is masked at the 0.75 km, a transitional level. The anti-cyclonic flow visible to the southeast
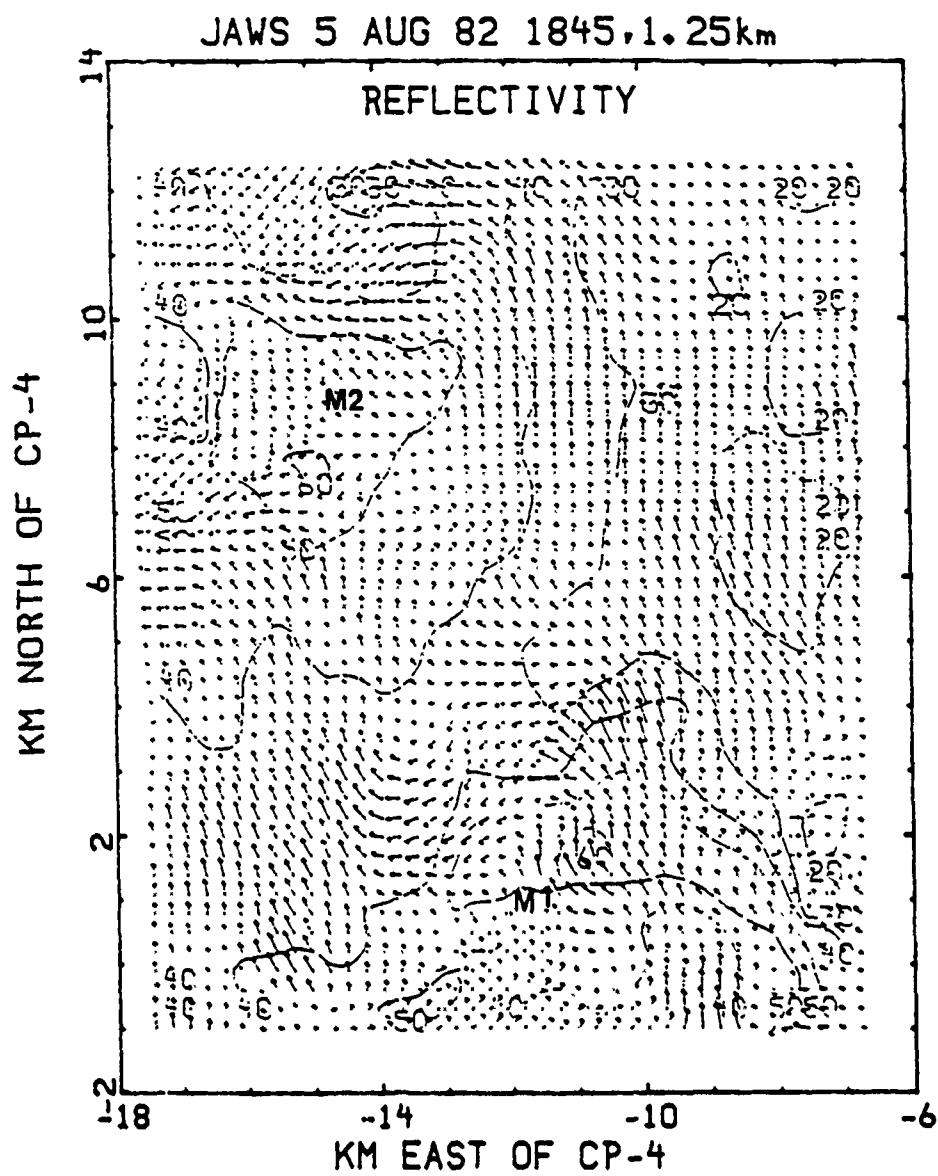
Fig. 5.10   Same as Fig. 5.1, except for 1.25 km.

of the grid domain (-8,-0.5) is more pronounced than at 1 km, and corresponds to the low-level cyclone attached to the southern flank of the surface gust front. A divergence of flow occurs on the southern flowing branch of M1's cyclonic ciculation approximately 2 km west of its main core. The westward branch of this split flow feeds into anticyclonic curvature while the eastern branch continues its cyclonic trek into the feeder tongue just south of M1. Mass inflow of dry air into M1 is from the southeast and southwest, while inflow for M2 occurs primarily from the north. The strength of M1 both absorbs and seemingly blocks the environmental wind thus forcing M2's circulation to draw its mass field from the north. Unlike Fujita's (1985) description of the misocyclone structure, which displayed the misocyclone's role as one of a collector of hydrometeors for the microburst to enhance precipitation loading, Coover (1988) proposed that the misocyclones act as pinwheels which funnel in and efficiently channel dry environmental air for the enhancement of evaporative cooling by ventilating the saturated downdraft. Entrained air is mixed within the downdraft creating evaporative cooling which aids the development of negative buoyancy production. Conclusively, circulation enhancment spawned by the misocyclones aloft aid to strengthen microburst affects triggered at lower levels.

The perturbation temperature field at 1.25 km (Fig. 5.11) exhibits warm core anomalies for both microburst events. Microburst M1 maintains a warm core (3°C) with surrounding cool air (-2- -3°C). The cold anomalies are the result of dry adiabatic expansion of the lower level environmental air channeled aloft within updraft areas.

Fig. 5.11 Same as Fig. 5.2, except for 1.25 km.
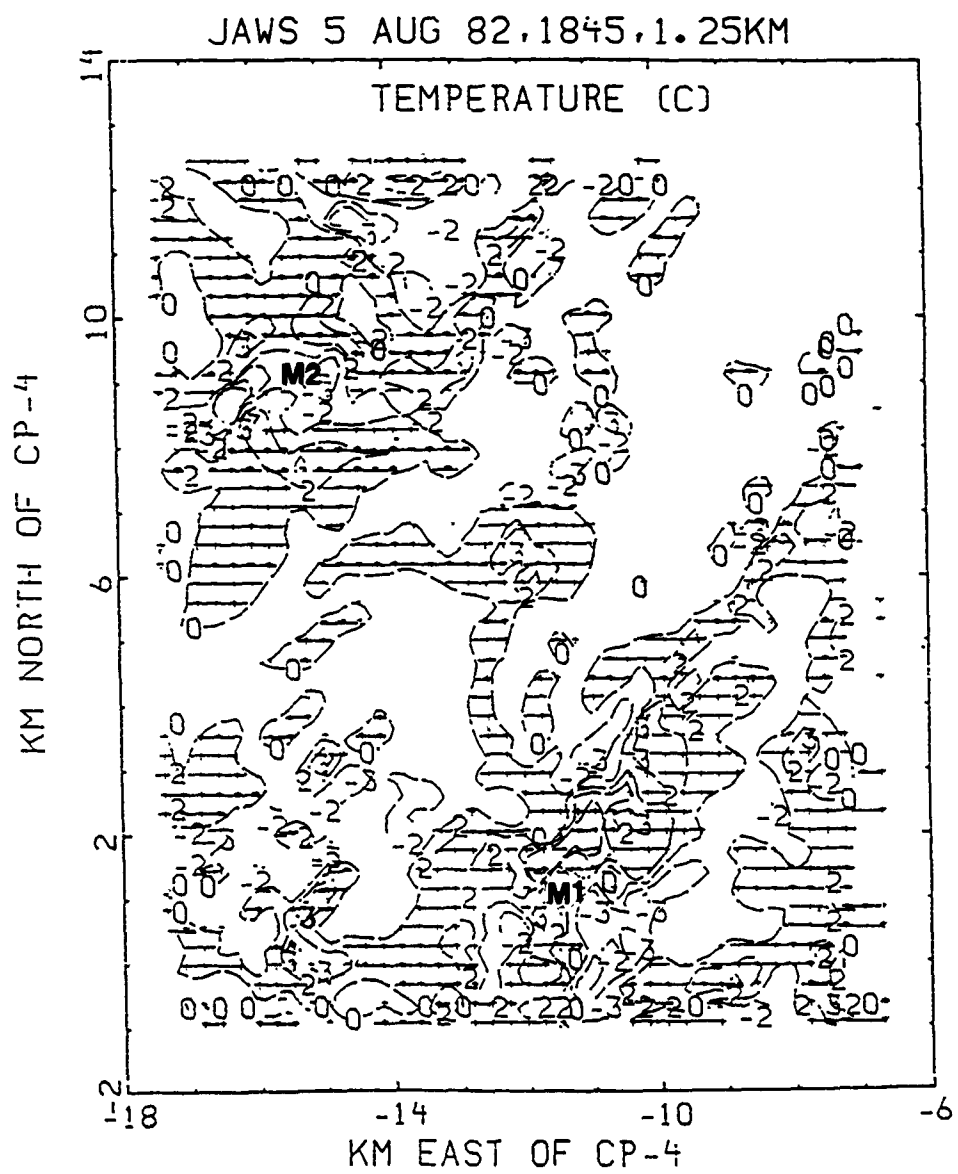
Similarly, cold temperature anamoly values associated with M2 vary between -2 and -3°C. Temperatures along the supposed gust front location remain neutral, while the cyclonic gyre west of M1 is also a warm core (3°). A warm anomaly (3°) exists with the relatively warm, dry environmental air entrained into the system. Microburst M2 is associated with cooling on its north side with a warm anomaly noted within the southward flowing entrained environmental air. It is interesting to note that relatively warm temperature values exist aloft within each parent storm, but low temperature values occur at lower levels. The warm anomalies are linked to compressional warming associated with rapid convergence and entrainment of environmental air being directed into the intense cyclonic circulation which, becomes the explosive descent of the microburst as indicated by the vertical velocity fields (Fig. 5.12). Note, however, that the warm anomalies quickly fade at 1 km and below, largely due to evaporating precipitation shafts, which regain a foothold within the microburst structural domain. Furthermore, a warm anomaly dominates an area of low reflectivity and upward motion as indicated by the vertical velocity field for 1.25 km and may be associated with the outflow from the bow echo. The bow echo itself is warm, but surrounded by cooler air, probably due to the entrainment process. Note the inflow of environmental air feeding into this feature from the southeast. As the warm environmental air becomes horizontally entrained, it maintains a warm anomaly due to slow rising and cooling until entering the major updraft. It does not encounter evaporative cooling until it enters the updraft and meets the surrounding saturated region of the updraft. Upon entering the main updraft, dry adiabatic ascent rapidly cools the
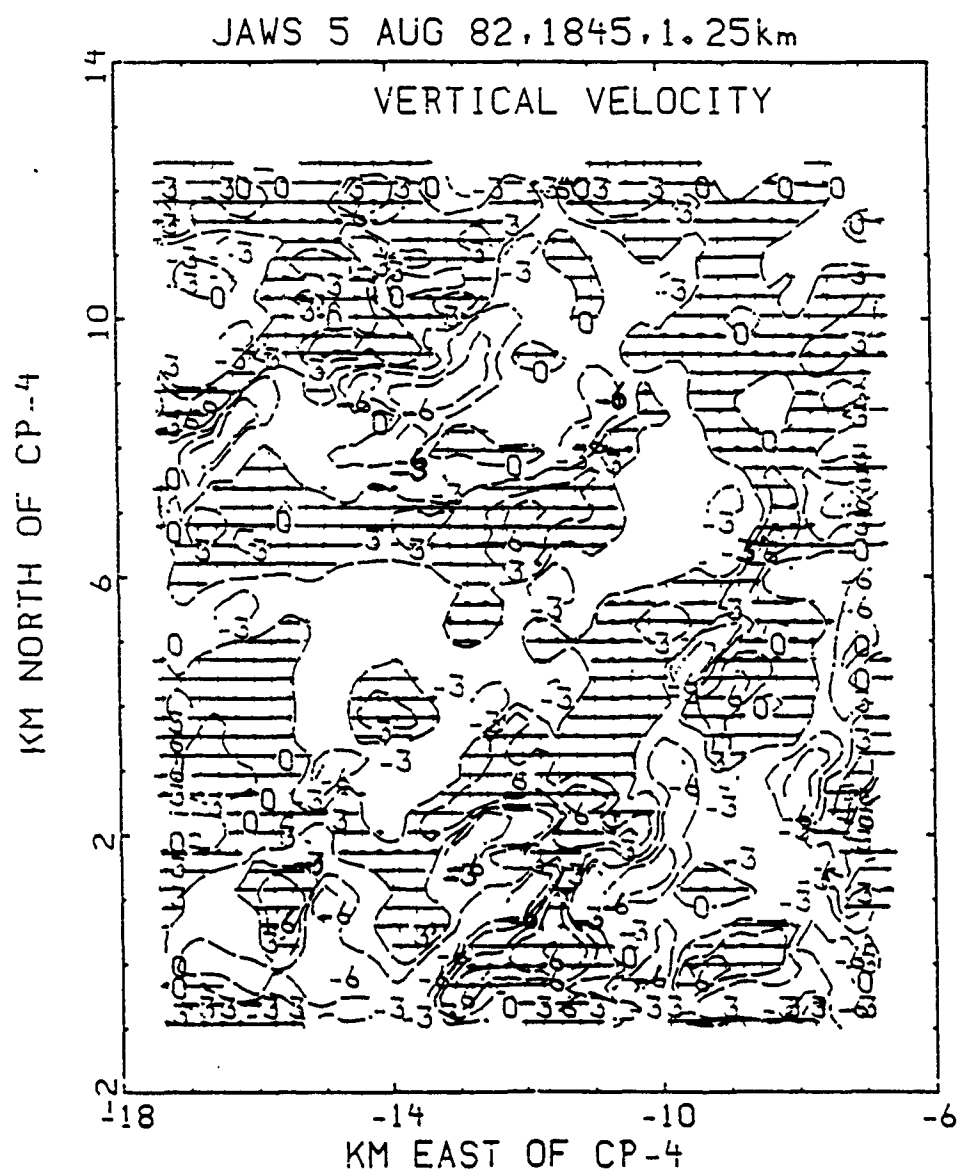
Fig. 5.12 Same as Fig. 5.5, except for 1.25 km.

54

region, thereby becoming a cold anomaly.

The vertical velocity field for 1.25 km characterizes each microburst event with downdraft values of -6 m s^{-1}. A semi-circle of updraft values (3 m s^{-1}) envelop M2 on its northwestern edge, while updraft values encircling M1's northeastern edge are 6 m s^{-1}. The cyclonic gyre due west of M1 maintains a downdraft speed of -6 m s^{-1} but reduces to -4 m s^{-1} at 1 km and nearly vanishes at 0.75 km. Thus, strong vertical convergence is occurring within this 0.5 km interval. Speeds of 3-6 m s^{-1} accompany the strong updrafts consistent at all levels within the central grid region. A strong updraft may also be found south of M1 with a speed of 6 m s^{-1}. Figure 5.13 displays the perturbation pressure pattern for this level where highest pressure is found near the southeast and northwest corners of the grid. Low pressure centers are found near the center of cyclonic circulation but offset by 2 km, which is consistent with all other studies. Mass flow therefore, is toward the cyclonic center from the surrounding region not associated with the cyclonic gyre, analogous to sedimentary erosion at points of low terrain. Microburst M1 carries a low pressure anomaly of -0.3 mb, while M2's low pressure center equates to -0.2 mb. Updraft regions which flank each microburst event maintain high pressure anomalies between 0.1 and 0.2 mb. The cyclonic gyre west southwest of M1 has a -0.1 mb low pressure value with a similiar high pressure value to its southwest.

Areas of downward motion are weakly warm at 1.25 km. Microburst M2 is a warm core event, while its main updraft is neutral to
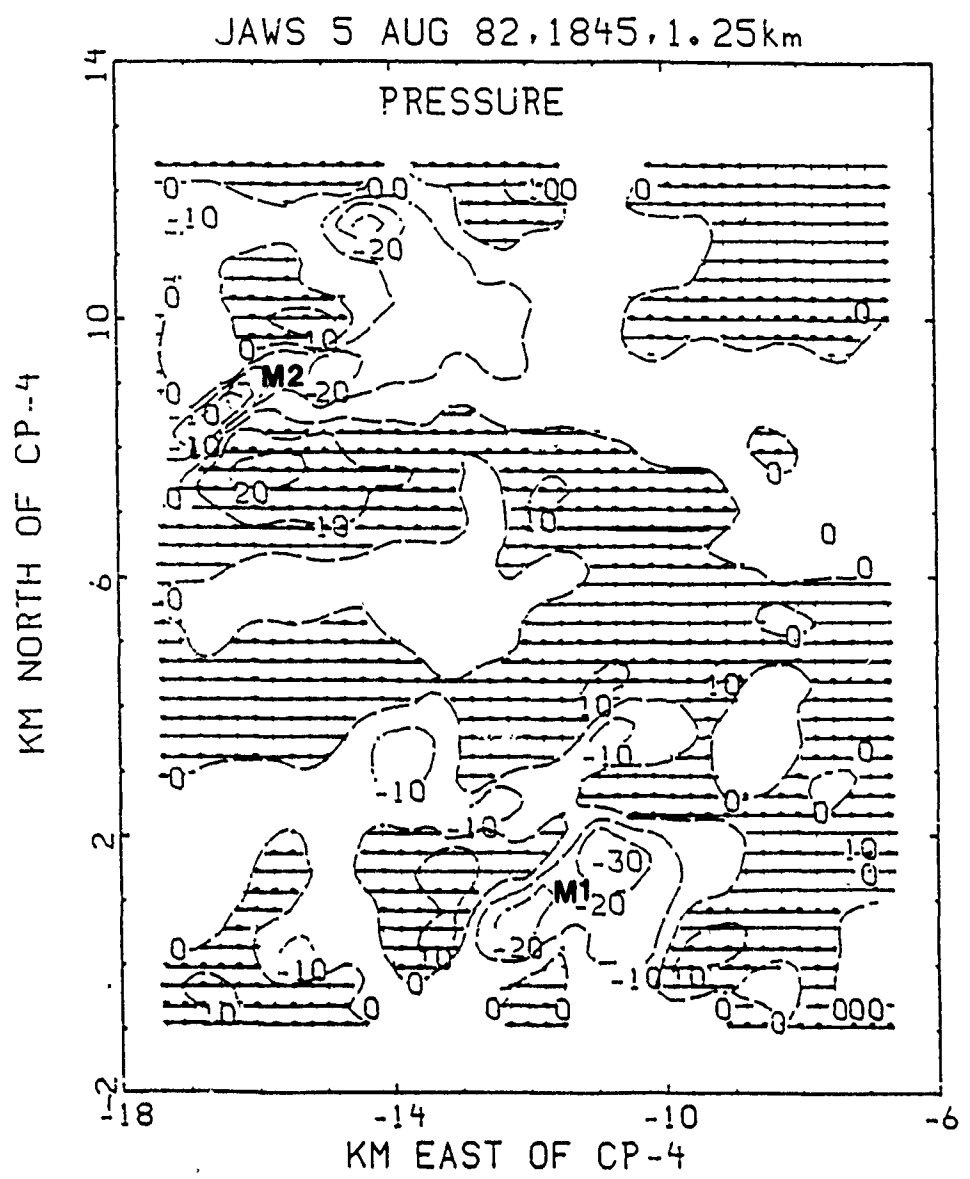
Fig. 5.13 Same as Fig. 5.3, except for 1.25 km.

slightly cool. A noted difference is the 2 km offset between M1 and its primary updraft. The offset difference in the M2 case is greater than 4 km. The larger cold anomaly of the updraft may influence the weak warm anomaly associated with the downdraft. The ascending cool air may be entrained into the misocyclone which may add additional negative buoyancy to the downdraft. A vivid portrait begins to emerge, consisting of intricate relationships between updrafts/downdrafts, divergent/convergent and high/low pressure anomalies. The entire pattern resembles that of a biological organism with self induced secondary and tertiary circulations, each drawing energy from the other. Microbursts may almost be thought of creature-like within the minds eye. Clearly, the 5 August 1982 1845 LST period reveals a complex system of several microbursts with associated misocyclones and gust fronts. Comparison of this data set with that obtained using the 500 m horizontal grid datum will unveil further structural features. It will hopefully provide an optimum grid scale for Doppler data analysis, and further identify the finer resolution of microburst phenomena and its PBL interactions.

5.2 Data Set Comparison: 250 m versus 500 m Grid Scale

Coover's (1988) previous study employed a 500 m horizontal grid spacing to investigate those features associated with the 1845 LST 5 August 1982 microburst case. Figure 5.14 displays the plain view of the 0.25 km level horizontal wind and reflectivity field using 500 m horizontal grid spacing. Distances are in kilometers from the CP-4 radar. Two microburst events are visible (M1 and M2) and occur near
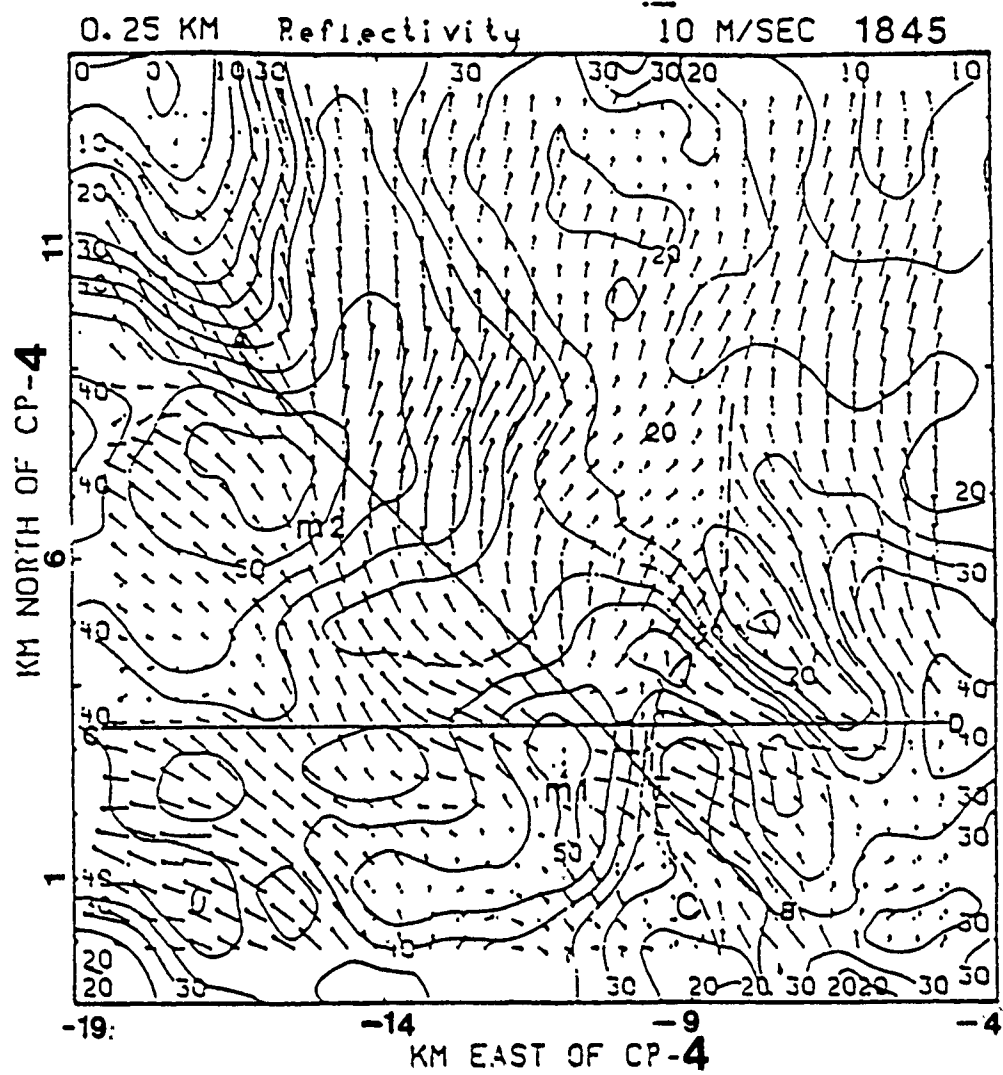
Fig. 5.14 Plan view: Horizontal wind and reflectivity field for the 5 August 1982, 1845 LST case using 500 m horizontal grid spacing at 0.25 km. (From Coover, 1988).

or within the areas of highest reflectivity, similar to the reduced grid fields, with values of 50 dBZ or greater. The dominant microburst feature, M1, is located at x=-11.5 and y=2. Microburst M2, however, is situated northwest of M1 near x=-15 and y=7. The larger scale analysis barely discerns M2's position, however, as it becomes nearly overwhelmed by M1's outflow boundary coupled with the environmental wind. Although, the 250 m grid scale analysis for this level clearly displays M2's associated outflow boundary, but its maximum divergence remains displaced downwind of its highest reflectivity core. Also, the gust front to the east of M1 is more concentrated at the smaller grid size and extends only 4 km in depth as compared to the 500 m datum which depicts the breadth of the gust front at 6-8 km. In addition, the cyclonic circulation discovered to the west-southwest of M1 at the refined grid scale goes unnoticed at the larger domain.

The perturbation temperature field (Fig. 5.15) for the 500 m grid scale at 0.25 km does verify the prescence of M2, but is only weakly shown. Cold temperature anomalies are found to be present for each microburst event at both scales of analysis, but slightly more pronounced at the smaller grid domain. One exception, however, is the warm anomaly located in the central portion of the grid associated · with strong updraft regions and strong downslope winds for both analysis scales. The warm anomaly in the central grid domain with 250 m grid spacing is smaller than at the larger scale, perhaps because adiabatic ascent is occurring more quickly at this scale which serves to cool the anamoly. Perturbation pressure features also appear more pronounced with the 250 m grid spacing than at the 500 m grid inter-
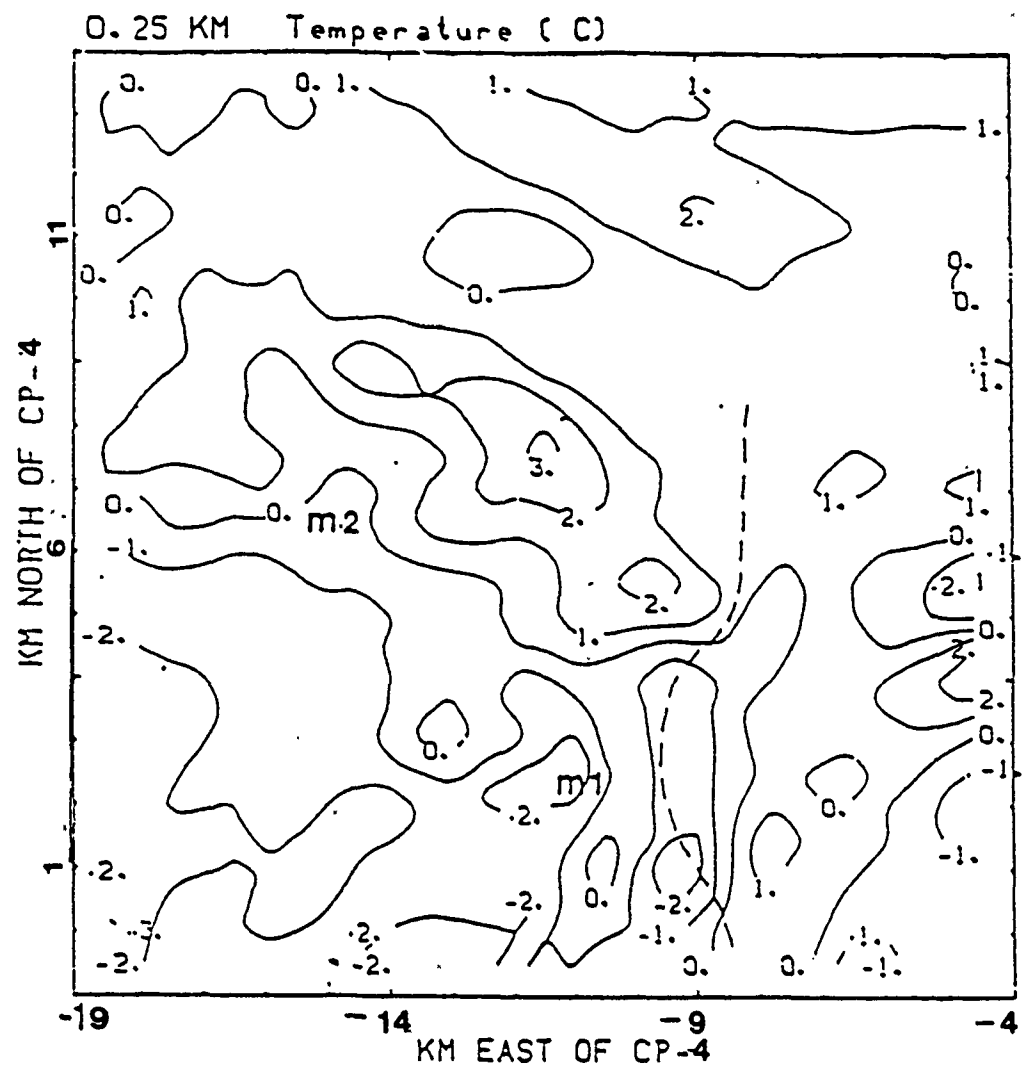
Fig. 5.15 Perturbation temperature for the 5 August 1982, 1845 LST case using 500 m horizontal grid spacing at 0.25 km. (From Coover, 1988).

60

val (Fig. 5.16).

Analysis of the 0.5 km level using 500 m horizontal grid spacing (Fig. 5.17) continues to depict both microburst regions and maintains the presence of the cyclonic circulation to the south of the gust front. However, the larger grid datum fails to identify the cyclonic gyre to the west-southwest of M1's position. Also, M2's outflow boundary at 0.5 km with 500 m grid spacing is again unpronounced, unlike the 250 m grid scale which readily identifies the divergent outflow boundary.

The vertical velocity field for this level at the 500 m grid interval (Fig. 5.18) displays values of -2 and -1 m s^{-1} for microbursts M1 and M2, respectively, as opposed to values of -3 and -2 m s^{-1} for M1 and M2 as obtained at the finer scale analysis domain. Both grid scale analysis' indicate the displacement or shift of M2's outflow boundary to its downwind side, attributed to the resultant coupling of the environmental mean wind for this level and M1's strong outflow boundary. Similarly, updraft regions are found to flank each microburst event as captured by both scales of analysis. The perturbation pressure fields for each analysis scales at this level clearly indicate the microburst regions as high pressure anomolies. However, the cyclonic circulation to the west southwest of M1 is found to correspond to a low pressure anomaly with the 250 m grid, but goes unnoticed at the 500 m horizontal grid scale. Thus, finer resolution of storm features again becomes visible at the smaller, 250 m, grid domain. Low pressure values generally occur along the gust front and surrounding each microburst, as indicated at both analysis scales.
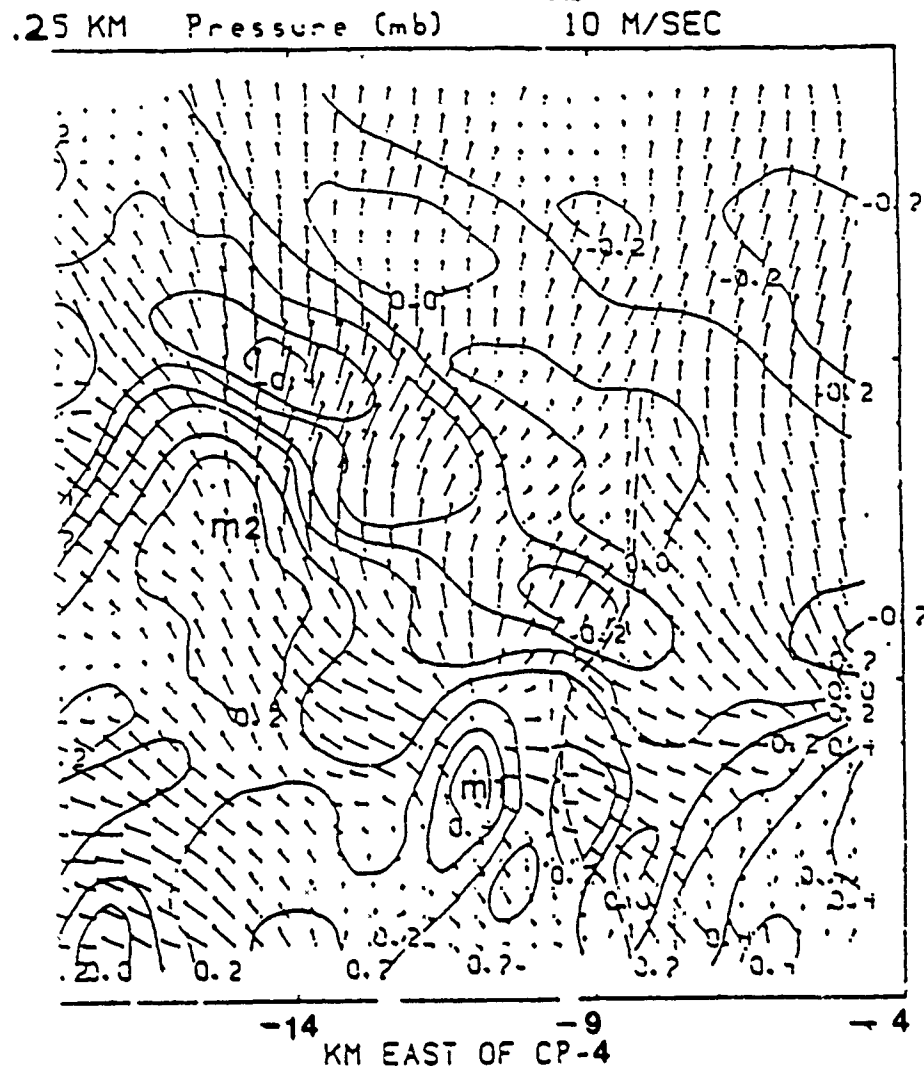
Fig. 5.16 Perturbation pressure field for the 5 August
1982, 1845 LST case using 500 m horizontal grid spacing
at 0.25 km. Units are in mb, to convert to Pa, multiply
by a factor of 100. (From Coover, 1988.).
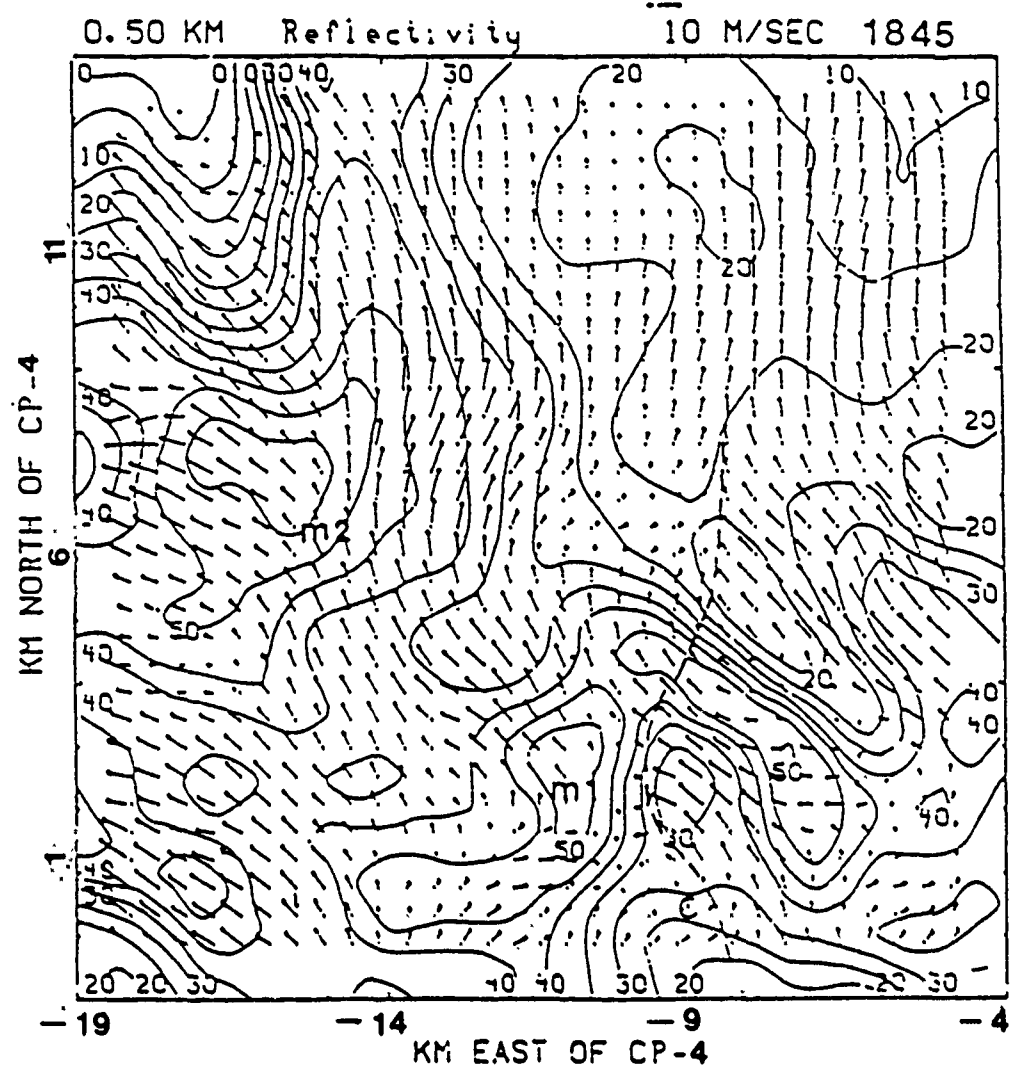
Fig. 5.17 Same as Fig. 5.14, except at 0.50 km.

63
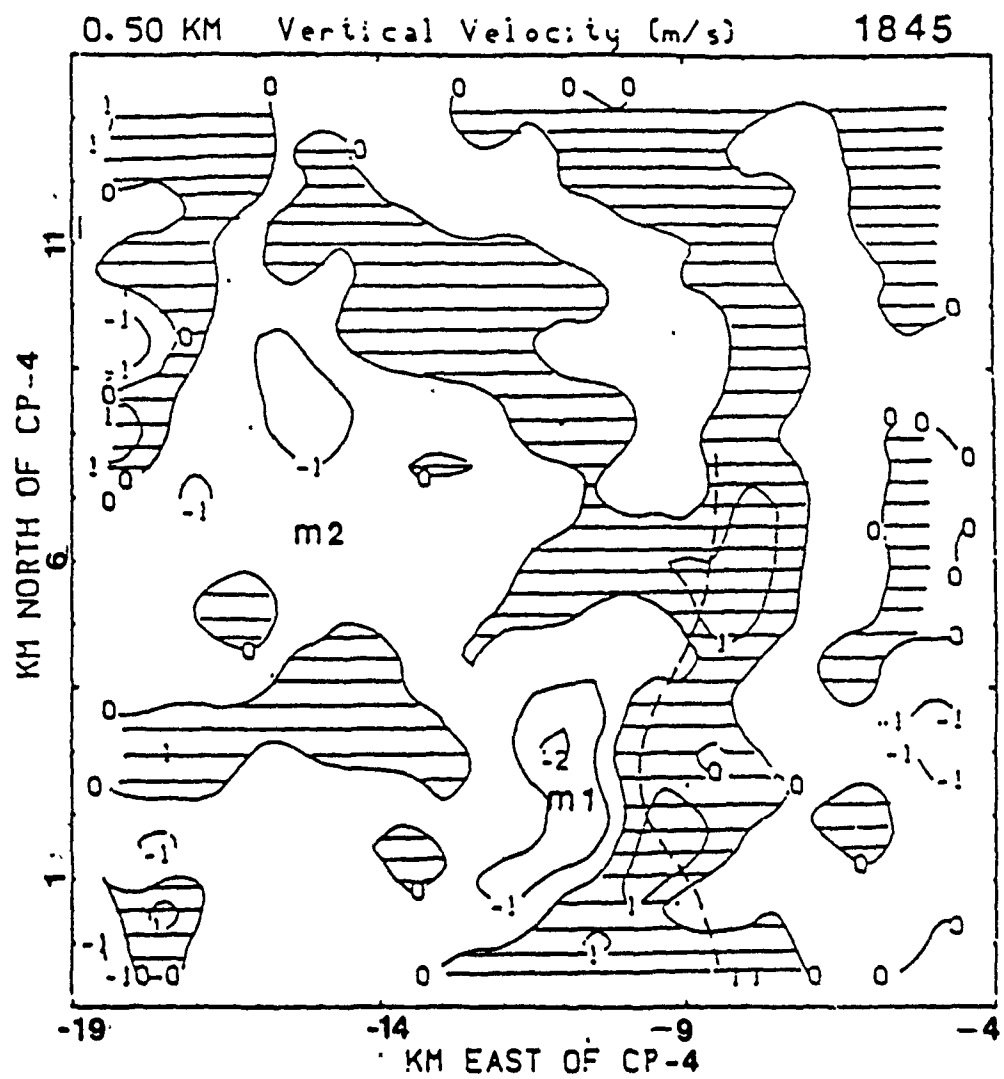
Fig. 5.18 Vertical velocity profile for the 5 August 1982, 1845 LST case using 500 m horizontal grid spacing at 0.50 km. (From Coover, 1983).

Figure 5.19 displays the perturbation temperature field for this level at the 500 m horizontal grid although less amplified than the smaller grid domain. It continues to feature relatively cold core anomalies in association with each microburst event, but unlike the 250 m analysis, the warm anomaly found in the central grid region diminishes; whereas it increases in magnitude and area at the smaller analysis grid domain. The terrain features, which aid to initiate strong downslope winds, trigger the warm anomaly and is more pronounced at this level using the 250 m horizontal grid than at the lowest level of that grid scale. This result is contrary to the 500 m grid datum which displays the warm anomaly to be most pronounced at its lowest level vice 0.5 km. Additionally, the cyclonic circulation on the gust front features a relatively cooler region as upward vertical motion increases; thereby, cooling the unsaturated inflow air by dry adiabatic expansion.

The horizontal wind field for 0.75 km using the 500 m grid scale is displayed in Fig. 5.20. Structural features associated with each microburst become less discernible at this level. Similar to the small grid datum, the environmental flow becomes more dominate; but at the smaller analysis scale, cyclonic motion begins to replace the M2 outflow boundary, a feature which is less obvious at the larger grid datum. None-the-less, vertical velocity fields continue to verify the prescence of each microburst event at both analysis scales. It becomes clear that the 0.75 km level is one of transitional change for storm composition. At the larger analysis scale, the cyclonic circulation south of the surface gust front is now replaced by an open cyclonic wave. Thus, it appears the cyclonic circulation extends only to about 0.75 km in depth, at this
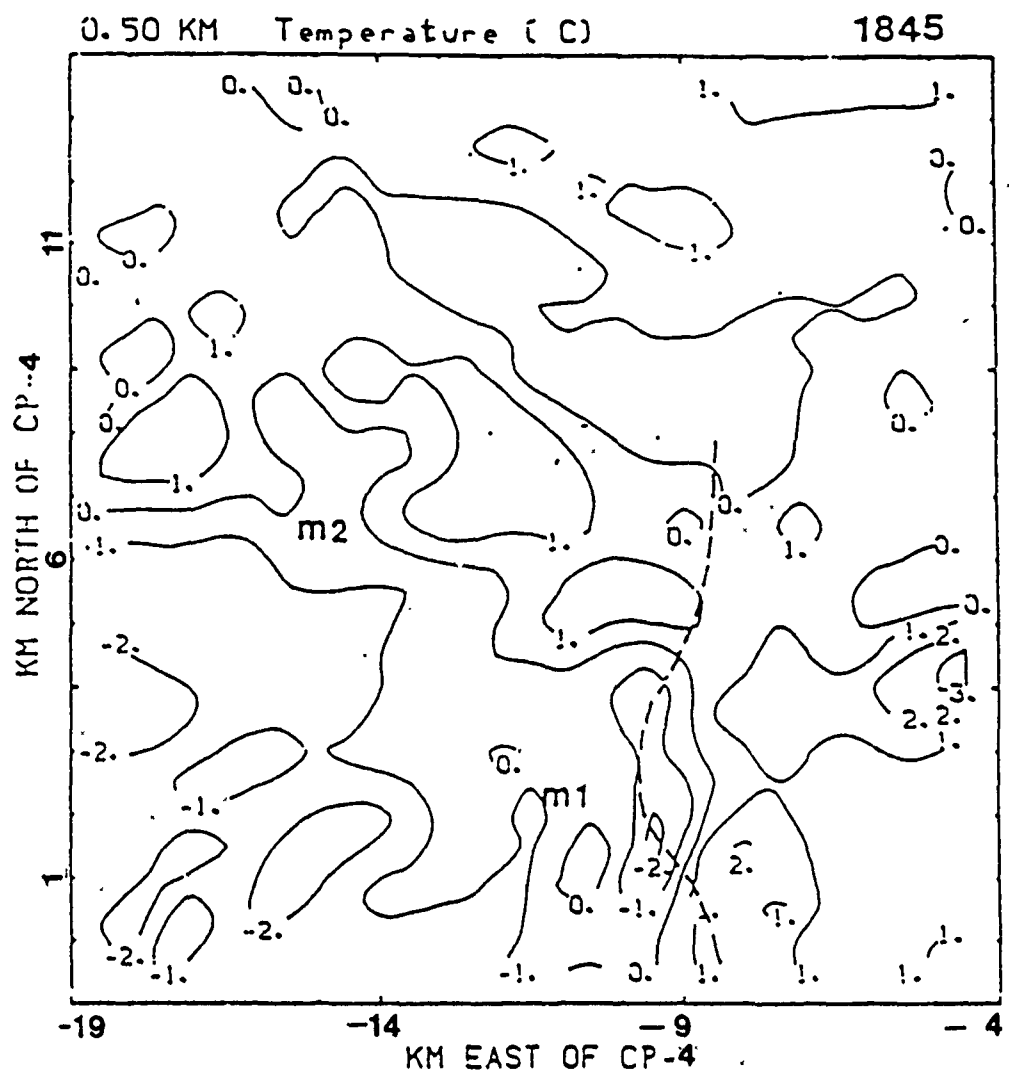
Fig. 5.19 Same as Fig. 5.15, except at 0.50 km.

.75 KM   Reflectivity   10 M/SEC 1845

KM EAST OF CP-4.. .
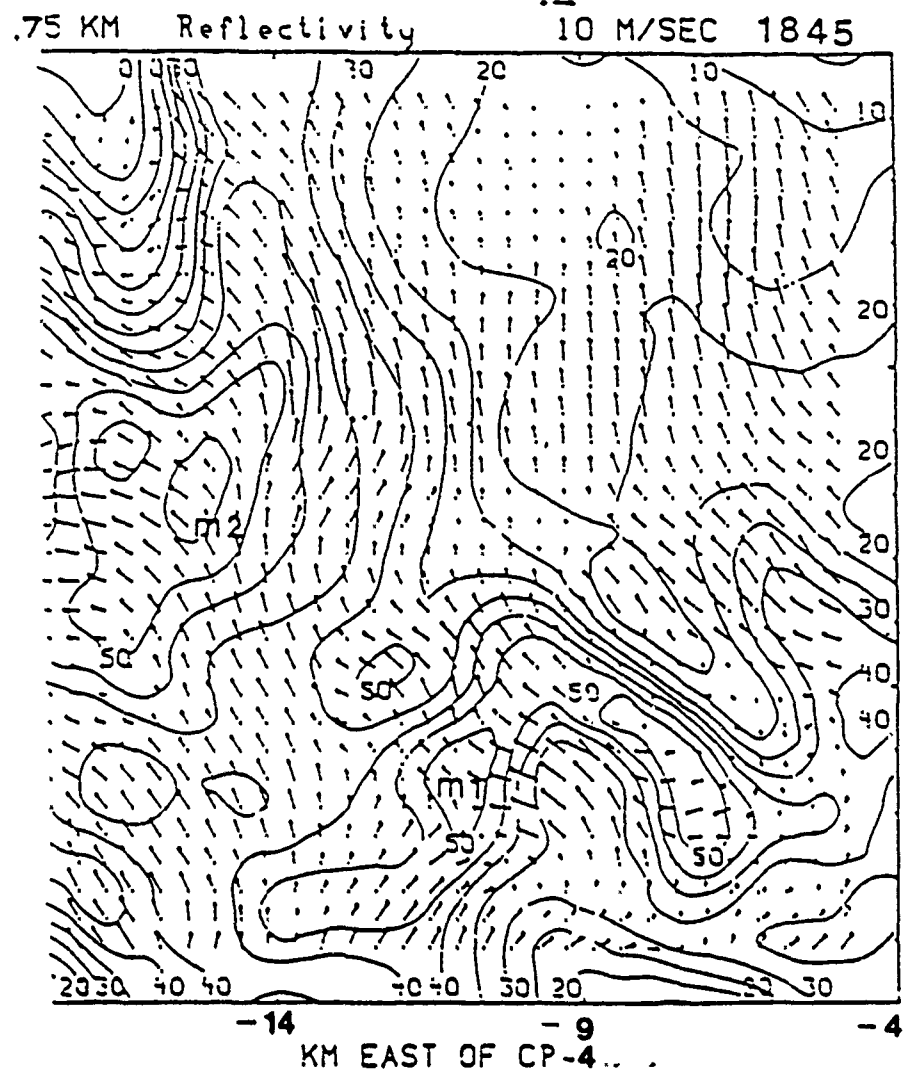
Fig. 5.20 Same as Fig. 5.14, except at 0.75 km.

larger analysis scale, with ever increasing radius of rotation. However, the smaller grid domain continues to depict the cyclonic feature associated with the spur of the surface gust front location. In fact, a feeder tongue begins to provide mass inflow from the west southwest of the cyclone which sweeps into the feature toward the south and wraps around well to the north under the full influence of cylonic circulation. Therefore, entrainment must be beginning to occur at the refined grid scale. Note also, the gust front position at the 250 m grid scale is shifted 1 km west northwest of its lower level position; while on the 500 m grid, the circulation south of the gust front tilts slightly west northwest with height. Indications are that dry air entrainment is occurring at this level when viewing the 250 m horizontal grid, but is notably absent at the larger grid domain. Inspection of those levels aloft will further identify like and unlike features of these storms as compared at separate grid scales of analysis.

The horizontal wind field for 1 km as obtained at 500 m horizontal grid spacing is shown in Fig. 5.21. Similar to the 250 m grid scale analysis, dry air entrainment begins to occur as observed by an increase in the crossing angle flow of environmental air from low to high relectivity cores associated with the descending precipitation shaft. Additionally, cyclonic curvature becomes established on the north sides of M1 and M2. At the larger grid scale, the cyclonic circulation south of the surface gust front in close proximity to M1 is notably absent; whereas, the finer grid domain vividly represents this feature. Also, the cyclonic circulation to the west southwest of M1, found masked at the 0.75 km level, begins to re-establishes itself at the 1 km level. Dis-
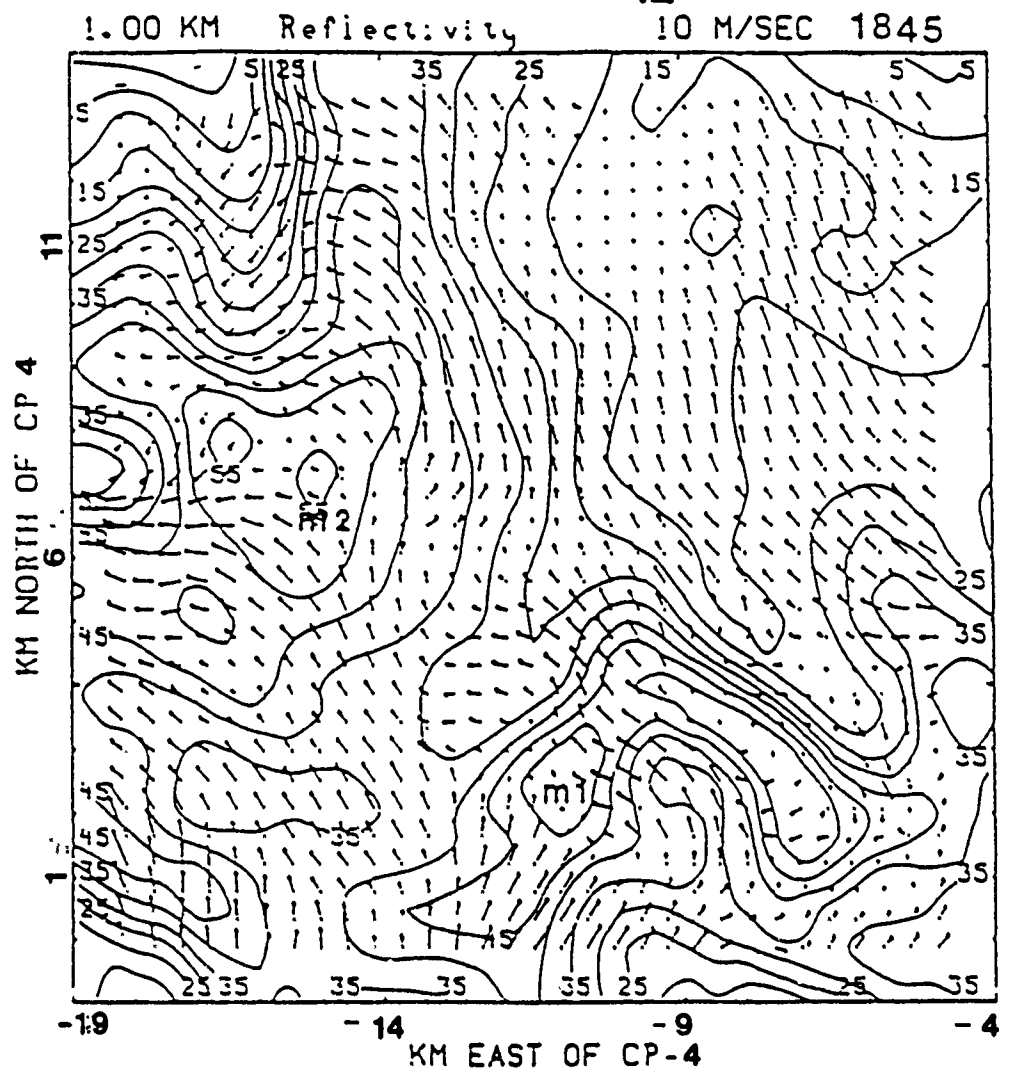
Fig. 5.21 Same as Fig. 5.14, except at 1.0 km.

tinct finger like appendages accompany both microburst features at each analysis domain. Examination of the 1.25 km level should reveal the complete picture of microburst structural features and their pattern toward phenomena evolution.

The upper-most storm level captured at the 500 m horizontal grid scale shows the structural features of both microburst events as more intense than at lower levels (Fig. 5.22). The finger like appendages associated with the dry air intrusions are broader than at 1 km and similar to the smaller grid scale analysis, the crossing angle of environmental air toward the higher reflectivity cores increase to almost a perpendicular angle. Cyclonic turning of the wind occurs around both microbursts with pronounced cyclonic circulation visible around M1. However, the smaller grid spacing clearly depicts strong cyclonic circulation with each microburst event. The smaller grid scale also vividly portrays the cyclonic circulation to the west south west of M1 at 1.25 km but, remains undetected at the larger scale analysis. The feeder circulations (mass inflow regions) at both scales of analysis remain from the south and southeast in M1's case, while becoming distinctly visible from the north northeast in M2's case. Thus, the strength of M1 continues to block the environmental wind, similar to a supercell thunderstorm forcing the high speed upper level winds to divert/split and channel around the circumference of the cell's core region thus further enhancing and perpetuating entrainment and roll tendencies. The result in our case is that M2 is forced to draw its mass field of inflow from the north.
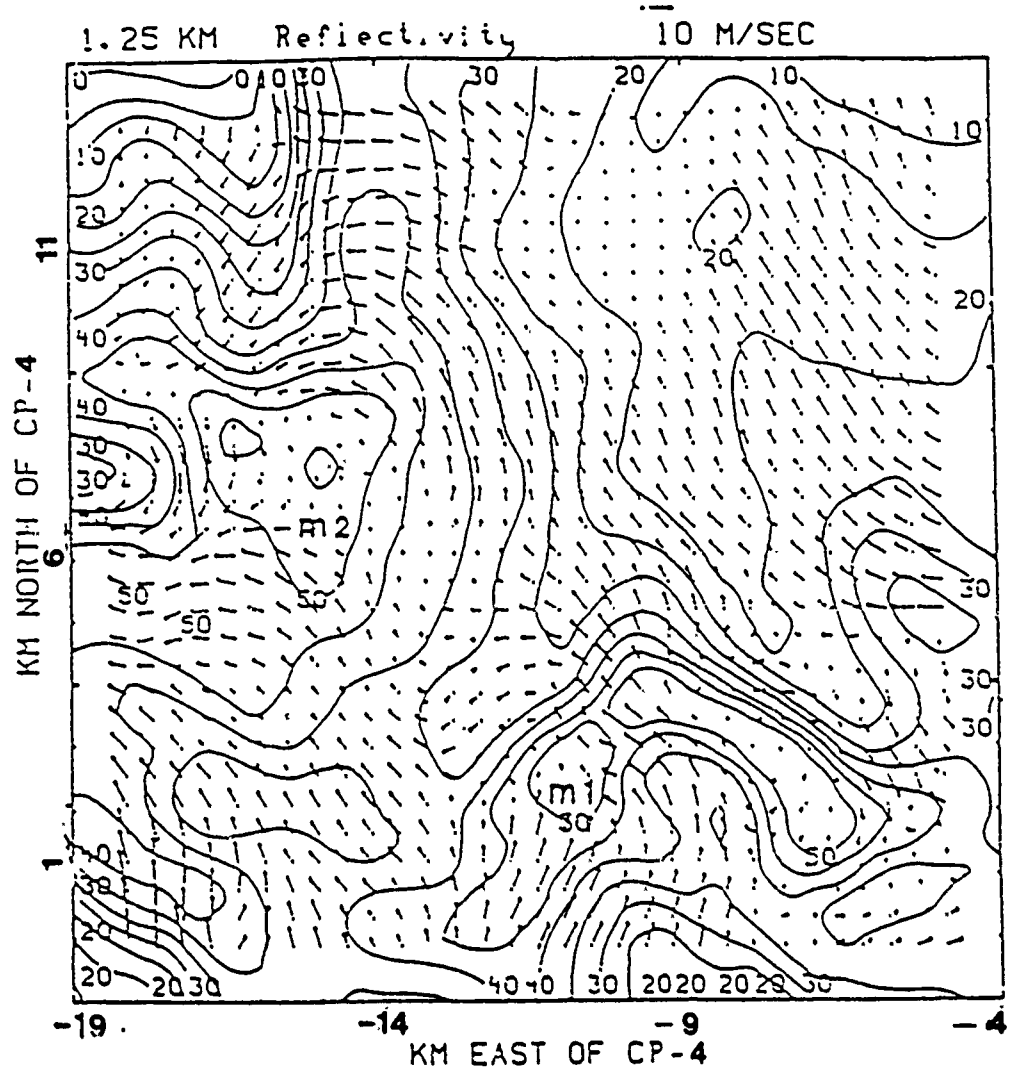
Fig. 5.22 Same as Fig. 5.14, except at 1.25 km.

Circulation enhancement aloft undoubtedly plays a significant role in microburst surface development by aggressively feeding the down-draft core with a rapid convergence of environmental air aloft, from all directions. Other differences found at this level using the smaller grid scale, but absent at the larger grid scale, include a westward shift of 1 km for M1's cyclonic core, a vivid projection of the surface cyclone attached to the southern flank of the surface gust front and the appearance of the cyclonic gyre to the west southwest of M1 depicted at each analysis level excluding 0.75 km. Note also, the divergent flow of M1's parent cyclone to its westward-southerly flowing side with the smaller grid scale. In part, this split in the flow is due to a shearing of the environmental wind, analogous to a supercell thunderstorm which forces the upper level flow around the solid body rotation of the updraft core.

The temperature field at this level for the 500 m grid scale is presented in Fig. 5.23. Both analysis scales depict warm cores for each microburst center with surrounding pools of relatively cool air. However, at the refined grid datum, temperature values are more pronounced than the larger scale. Temperatures along the gust front at the 250 m grid spacing are seemingly neutral but, slightly cool at the 500 m grid spacing. Also, the cyclonic circulation to the south southwest of M1 at 250 m resolution maintains a warm temperature anomaly, while its location at 500 m resolution has a neutral value. The warm anomaly found on both grid intervals, i.e., (-9,5) at 500 m resolution; and (-10,4.5) at 250 m resolution, which dominates low reflectivity areas and upward motion (Fig. 5.24 at 500 m resolution)
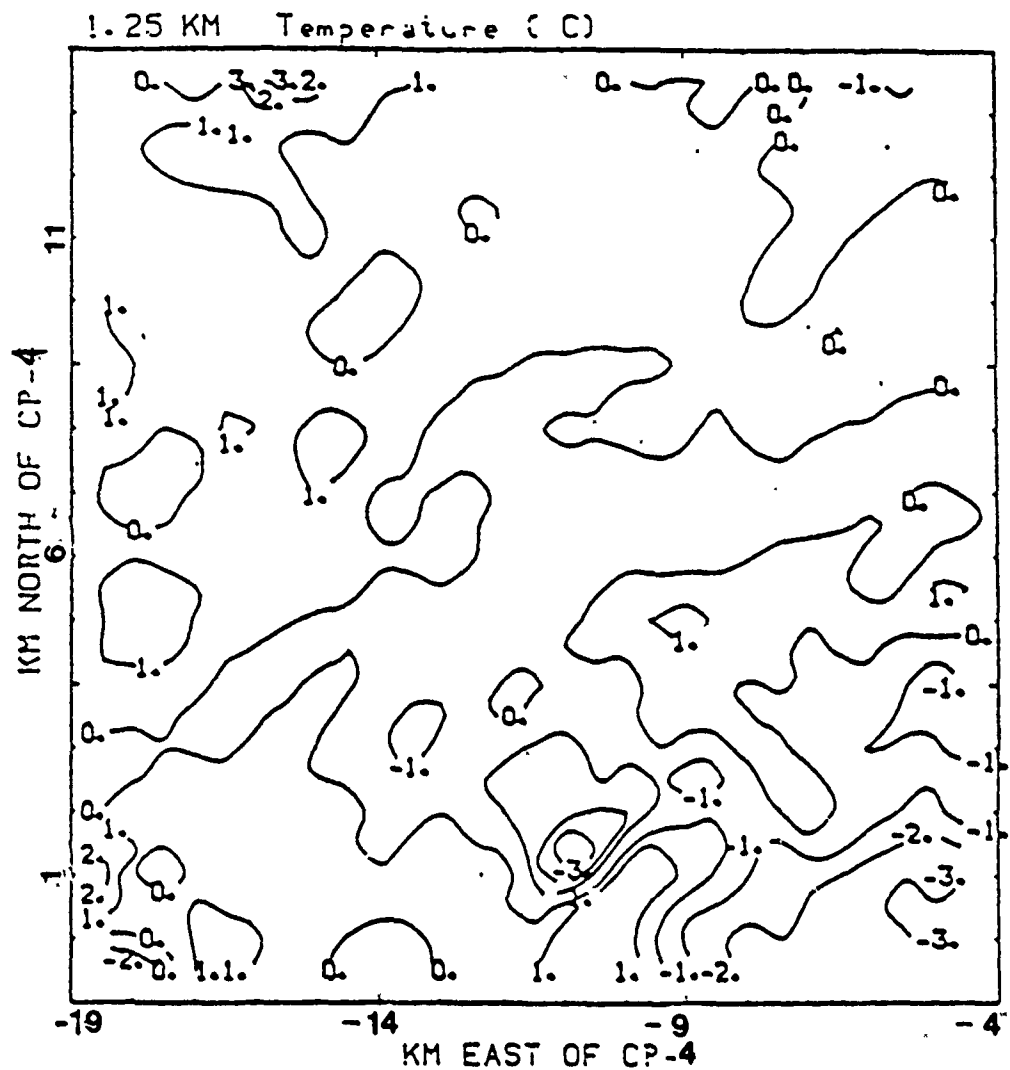
Fig. 5.23   Same as Fig. 5.15, except at 1.25 km.

73
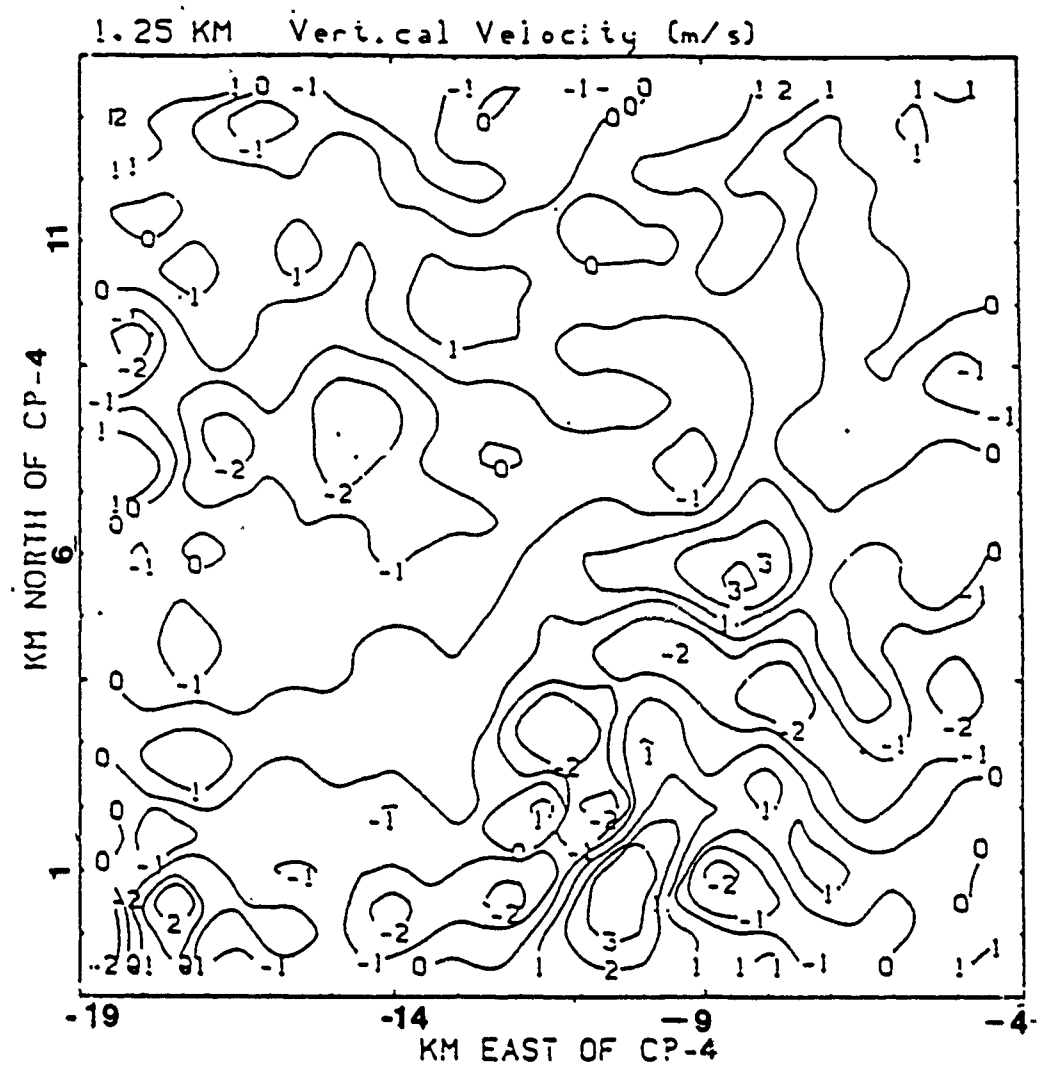
Fig. 5.24 Same as Fig. 5.18, except at 1.25 km.

74

may be associated with the bow echo. As discussed previously (section 5.1), cool air surrounds the warm anomaly probably due to entrainment. Upon entering the main updraft, dry adiabatic ascent rapidly cools the region, thereby becoming a cold anomaly. Note also, vertical velocity values obtained at the refined grid datum completely dominate those values found at the 500 m resolution scale increasing at times a full order of magnitude. Downdraft speeds at the 500 m scale associated with M1 and M2 are - 2-3 m s^{-1}, but at the 250 m scale those values increase to - 3-6 m s^{-1} for each respective microburst. Likewise, updraft regions envelop both microburst events at each horizontal datum. The cyclonic circulation to the west southwest of M1 detected at the 250 m datum carries a downdraft speed of -6 m s^{-1}, but this value quickly reduces in magnitude at the 1 km level and practically vanishes at 0.75 km.

Similar to the 250 m grid spacing analysis, the perturbation pressure pattern for this level (Fig. 5.25) clearly associates both microburst events and parent cyclonic circulation regions with characteristic low pressure. High pressure anomalies are found near the southeast and northwest corners of the grid. Perturbation pressure values appear more pronounced at the smaller analysis scale than at the larger one. The cyclonic gyre to the west southwest of M1 maintains a low pressure anomaly with a similar high pressure value to its southwest.

The three-dimensional nature of microburst, time excluded, begins to unfold in the vertical cross section analysis of each storm. The vertical cross section perspective coupled with the horizontally disected lev-
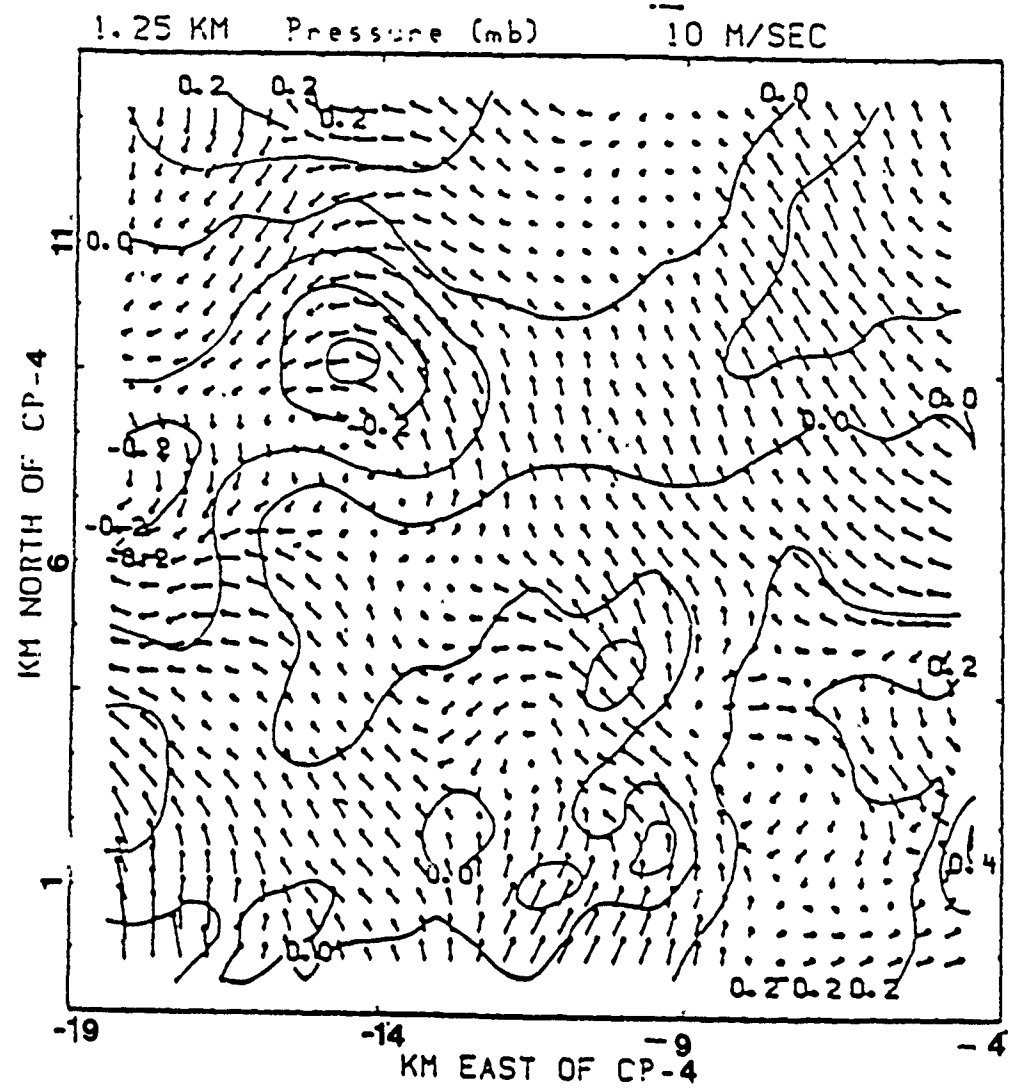
Fig. 5.25 Same as Fig. 5.16, except at 1.25 km.

els presented earlier, clarifies those features of microburst. Figures 5.26 and 5.27 display the west to east (W-E) cross section of the mean wind and reflectivity field using the refined grid datum for microbursts M1 and M2, respectively. Features compare nicely with the previous study which used the larger grid datum (Fig.5.28) and well diagram each microburst event with characteristic downdraft areas and complimental updraft regions, each within areas of highest reflectivity. At the larger analysis scale, the field of flow is generally right (east) to left (west), but the refined grid datum clearly reveals a more peturbed field of eddy motion within and around each microburst much more distinctly. Both analysis scales depict the gust front region to the east of M1. Microburst M2 however, is well pronounced at the smaller grid scale as opposed to the larger grid and the microburst itself resembles a cat eye. Turbulent circulation results from the storm outflow and environmental inflow exchanges (Lin and Hughes, 1987). Hence, a secondary circulation becomes vividly apparent and initiates a recycling of the mass outflow driving it into the updraft east of M2, which, in turn, is re-fed into the environmentally entrained air to be affectively channeled back into M2's central downdraft core.

The W-E cross sections of vertical velocities for these storms (Figs. 5.29 and 5.30) add further credence to those observations noted above. Microburst M2 carries a -3 m s^{-1} value to near surface level before being caught in the updraft to its east and driven aloft with a speed of 3 m s^{-1}. Microburst M1 however, maintains downdraft strength values of -4 m s^{-1} with corresponding updraft speeds, 1 km to its east associated with the surface gust front, between 2 and 4 m s^{-1}. The

REFLECTIVITY FIELD

JAWS 1845L Y=2!(M dx=.25km ⟶ 10 M/SEC
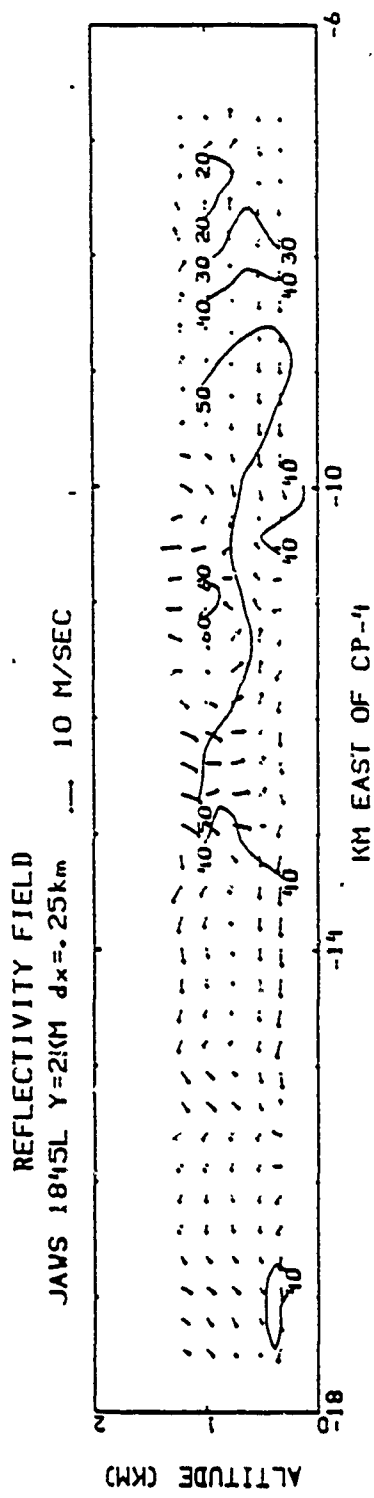
Fig. 5.26 West to East (W-E) vertical cross-section of the mean wind and reflectivity field for the 5 August 1982, 1845 LST case using 250 m horizontal grid spacing for microburst M1.

REFLECTIVITY FIELD
JAWS 1845L Y=2KM dx=.25km ⟶ 10 M/SEC

KM EAST OF CP-4

ALTITUDE (KM)
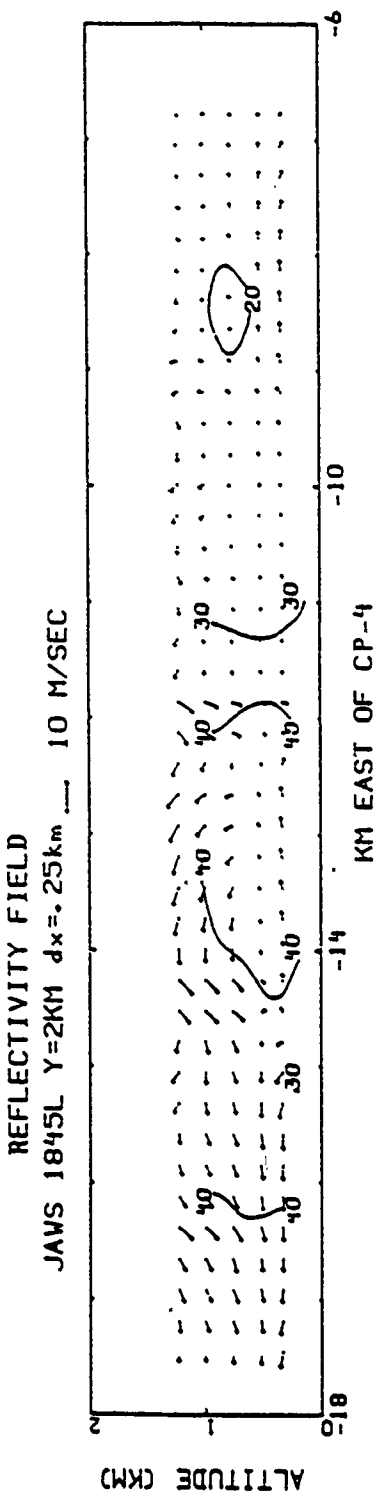
Fig. 5.27 Same as Fig. 5.26, except for microburst M2.
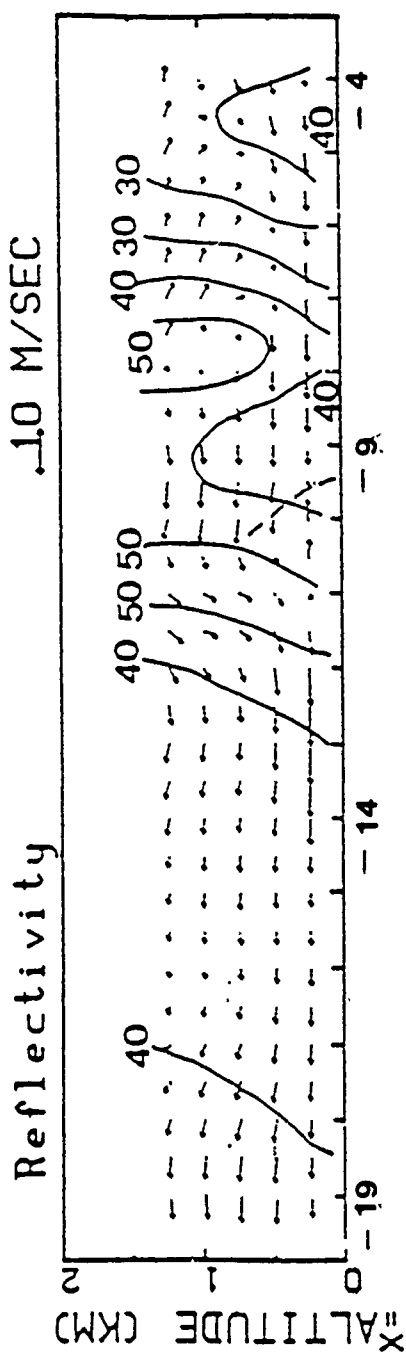
Fig. 5.28 Same as Fig. 5.26, except using 500 m horizontal grid spacing (From Coover, 1988).

VERTICAL VELOCITY FIELD
JAWS, 1845L, Y=2KM, dx=.25km
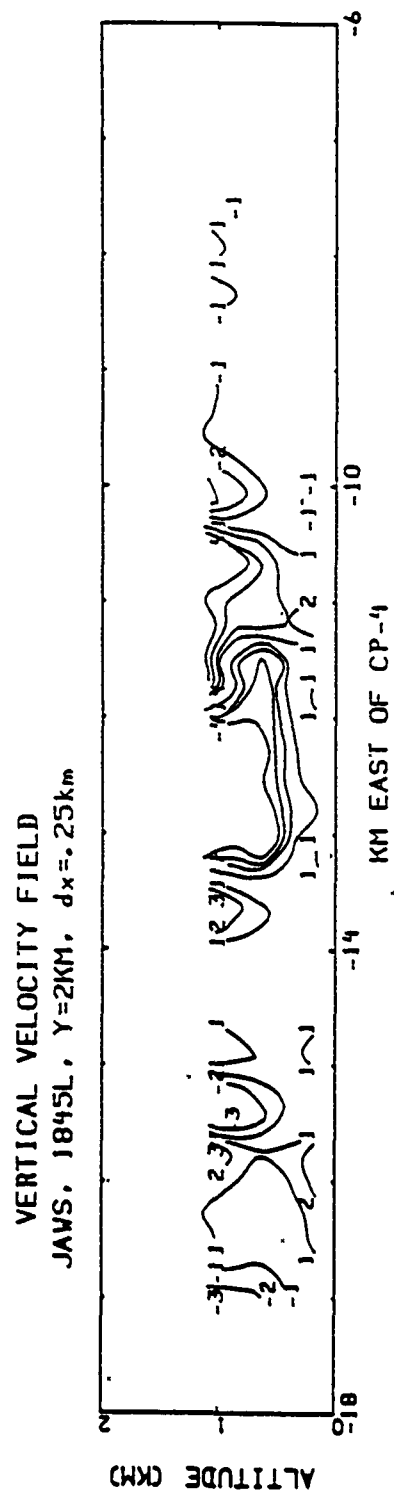
Fig. 5.29 W-E vertical cross-section of vertical velocity
for the 5 August 1982, 1845 LST case using 250 m horizon-
tal grid spacing for microburst M1.

81

VERTICAL VELOCITY FIELD
JAWS 1845L Y=2KM dx=.25km
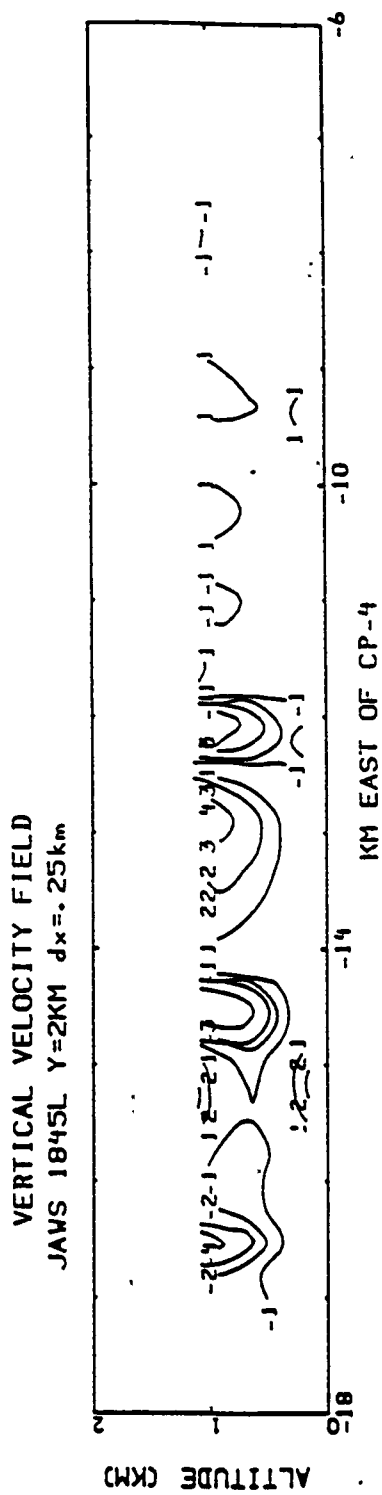
Fig. 5.30 Same as Fig. 5.29, except for microburst M2.

82

smaller analysis datum depicts microburst features much more vividly and with stronger values than those obtained at the larger grid scale which carries values of only -3 and -2 m s^{-1} for each storm accordingly (see Coover 1988). Thus, the vertical velocity profiles distinguish the overall storm intensity at the refined analysis scale and at times overshadow the larger grid datum a full order of magnitude.

Perturbation pressure cross sections for each storm (Figs. 5.31 and 5.32) typify high pressure anomalies at surface level, within the main downdraft core regions, with characteristic low pressure anomalies aloft in association with parent misocyclones. Misocyclone values are -.3 mb for M1 and -.2 mb for M2 accordingly. Additionally, the surface high pressure anomalies in association with M1 and M2 trigger a reversal in the mean flow pattern, just east of each event, due to the perturbed state of the pressure gradient. This feature is less pronounced at the larger grid datum (see Coover, 1988). None-the-less, this study indicates the smaller grid resolution does a better job than larger analysis scales and that perturbation pressure fields act as an accelerating force similar to findings in studies performed by Lin and Coover (1988) and Lin et al. (1986).

The W-E perturbation temperature cross sections for the refined analysis scale reveal uncharacteristic warm value anomalies aloft with cold core surface values associated with each microburst event as discussed earlier (Figs. 5.33 and 5.34). Compressional warming is at least in part responsible for the warm anomalies near misocyclone level, due to the rapid convergence of mass into their core regions. Precipitation

PRESSURE FIELD

JAWS, 1845L, Y=2KM, dx=.25km
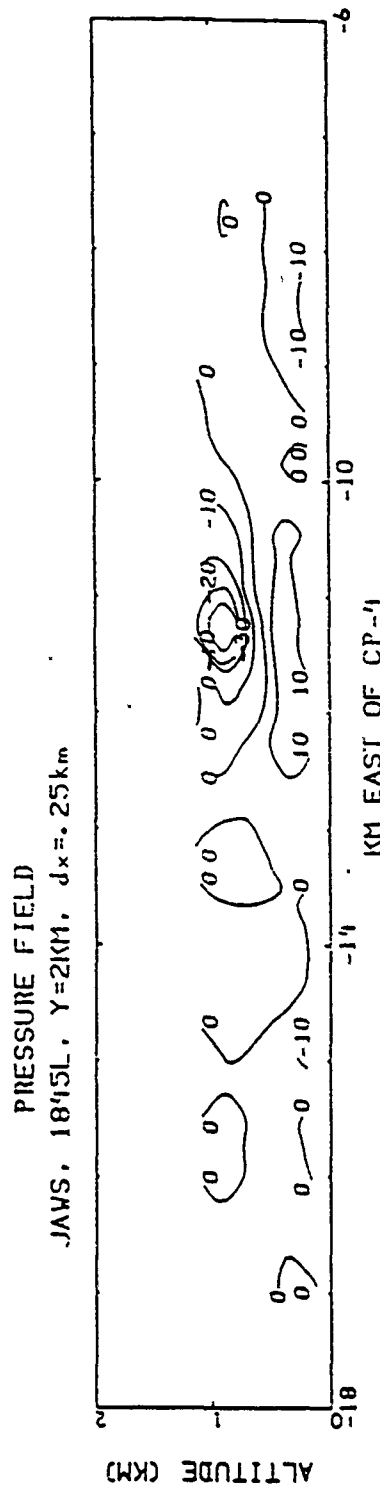
Fig. 5.31 W-E vertical cross-section of perturbation pressure for the 5 August 1982, 1845 LST case using 250 m horizontal grid spacing for microburst M1. Units are in Pascals where 1 Pa equals .01 mb.

PRESSURE FIELD
JAWS 1845L Y=2KM dx=.25km
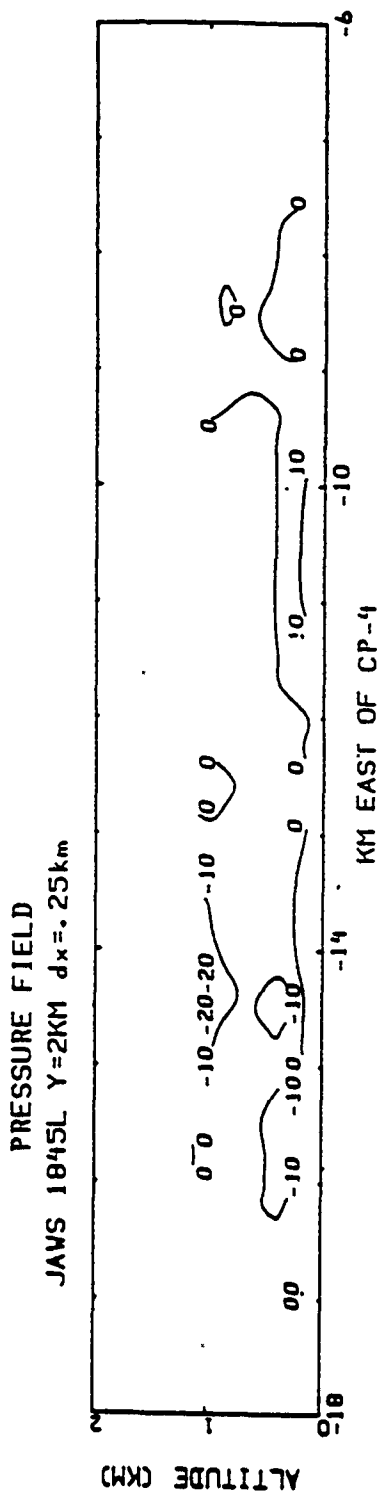
Fig. 5.32 Same as Fig. 5.31, except for microburst M2.

TEMPERATURE FIELD

JAWS. 1845L. Y=2KM. dx=.25km


ALTITUDE (KM)

KM EAST OF CP-4
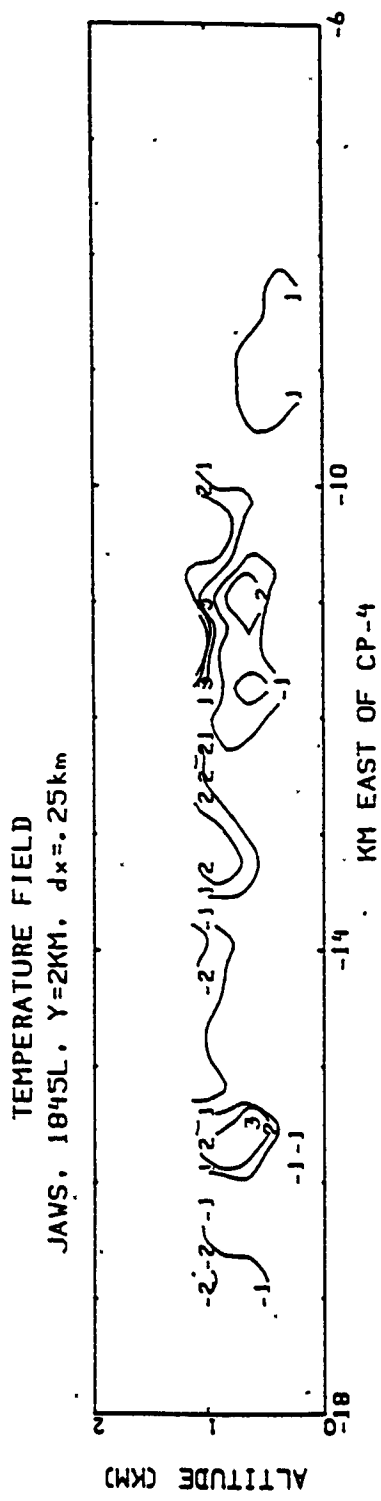
Fig. 5.33 W-E vertical cross-section of perturbation tem-
perature for the 5 August 1982, 1845 LST case using 250 m
horizontal grid spacing for microburst M1.
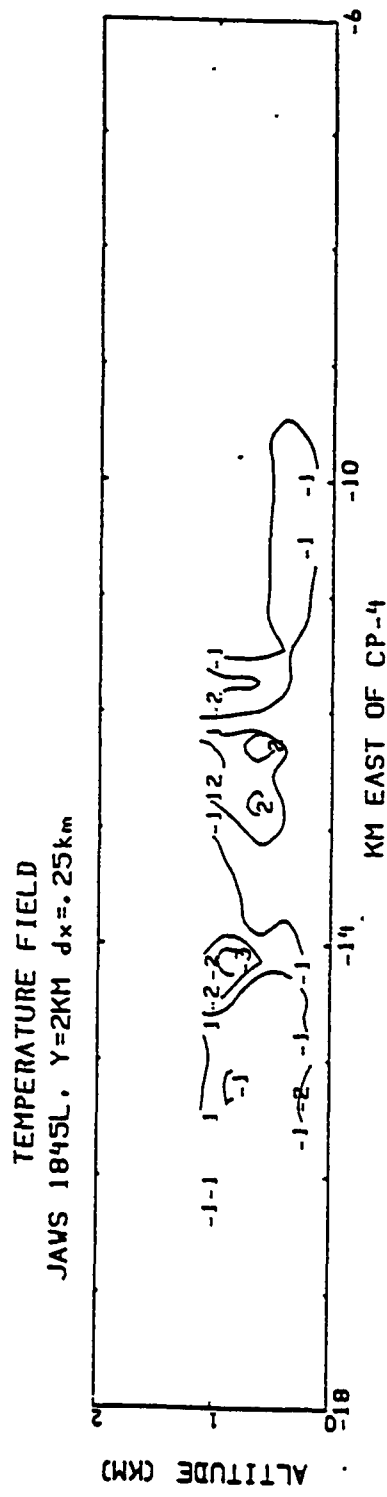
Fig. 5.34 Same as Fig. 5.33, except for microburst M2.

loading and subsequent cooling within each microburst downdraft is responsible for the cold core anomalies at surface level. Additionally, the cool values within the gust front region are believed due to dry adiabatic ascent and expansion.

Both analysis sets have revealed the delicate nature of microburst phenomena and the nominal respect which must accompany this aviation hazard. It was found that the smaller horizontal grid domain (250 m spacing) often provided better resolution of those features under investigation. It becomes clear that Doppler radar is the primary instrument to diagnose and forecast severe weather occurrence to include microburst and low-level wind shear events.

6. CONCLUSIONS

Multiple case studies, e.g., McCarthy et al. (1984), Coover (1988), ect., establish the diversity of the microburst phenomena and the role played by the parent misocyclone with each individual storm. It was found that by examining several microburst events, obtained via JAWS data sets, at a refined horizontal grid datum, structural features became more visible and readily identifiable. Additionally, vertical velocity values increased between one and tenfold at the smaller grid scale than discovered at the larger horizontal grid datum. Interactions between microburst phenomena and the PBL clearly reveal the reality in the aviation hazard associated with this forceful display of nature. Perturbation pressure gradients thus act as accelerating forces vigorously driving masses of environmental air from one level to another, similar to the pulsating rhythm of the human respiratory system.

Examination of both analysis data sets reveals useful knowledge toward understanding the phenomena of microburst and their PBL interactions. It was discovered that several features undetected at the larger grid scale became vividly apparent at the refined horizontal grid datum. Additionally, most features discovered became strikingly more apparent, both in magnitude and appearance than the previous study. None-the-less, inspection of each data set allowed the author to gain a most appreciable sense of awareness toward scientific research and the capabilities of Doppler weather radar.

Through data set comparison of these same storm volumes using different horizontal grid datums, both the current study using 250 m grid scale and the previous study which used the 500 m horizontal grid scale, it is recommended and proposed that a horizontal grid scale domain of 250 m be employed for optimum Dual-Doppler radar analysis.

The entire system, involving microburst phenomena, may be equated to a series of checks and balances, similiar to the growth, nourishment and thrashing of wheat to produce the final product for consumption. Microburst phenomena are thus categorically personified in a single and unique context for each individual event. One is forced to respect such phenomena and hope that the implementation of new technologies and more focused education will prevent human fatality associated with microburst throughout the duration of time!

BIBLIOGRAPHY

Armijo, L., 1969: A theory for the determination of wind and precipitation velocities with dual-Doppler radars. J. Atmos. Sci., 26, 570-573.

Barnes, S., 1973: Mesoscale objective analysis using weighted time series observations. NOAA Tech Memo. ERL-NSSL-62, 60pp., 1973. (Available from National Severe Storms Laboratory, Norman, OK, 73069).

Bohne, A. R., and R. C. Srivastava, 1976: Random errors in wind and precipitation fall speed measurement by a triple Doppler radar system. Preprints, 17th Radar Meteorology Conf., Seattle, Amer. Meteor. Soc., 7-14.

Brandes, E. A., 1984: Relationship between radar derived thermodynamic variables and tornadogenesis. Mon. Wea. Rev., 112, 1033-1052.

_____, 1978: Mesocyclone evolution and tornadogenesis: Some observations. Mon. Wea. Rev., 106, 995-1011.

_____, 1977: Gust front evolution and tornadogenesis as revealed by Doppler radar. J. Appl. Meteor., 16, 333-338.

Brown, J. M., K. R. Knupp, and F. Caracena, 1982: Destructive Winds from Shallow, High Based Cumulonimbi. Preprints, 12th Conf. on Severe Local Storms, San Antonio, Tx. Amer. Meteor. Soc., 272-275.

Chong, M., P. Amayenc, G. Scialom, and J. Testud, 1987: A tropical squall line observed during the COPT 81 experiment in West Africa. Part I: Kinematic structure inferred from dual-Doppler radar data. Mon. Wea. Rev., 115, 670-694.

_____, and J. Testud, 1983: Three-dimensional wind field analysis from dual-Doppler radar data. Part III: The boundary condition: An optimum determination based on a variational concept. J. Climate Appl. Meteor., 22, 1227-1241.

Coover, J. A. Jr., 1988: Kinematic and Dynamic studies of microbursts in the sub-cloud layer derived from JAWS dual-Doppler radar for a Colorado thunderstorm. Ph.D. Dissertation, St. Louis University, 225 pp.

Doviak, R. J., and Zrnic, 1984: Doppler radar and weather observation. Academic Press, Inc., 458 pp.

_____, P. S. Ray, R. G. Strauch, and L. J. Miller, 1976: Error

estimation in wind fields derived from dual-Doppler radar measurements. *J. Appl. Meteor.*, 15, 868-878.

Elmore, K. L., J. McCarthy, W. Frost, and H. P. Cheng, 1986: A high resolution spatial and temporal multiple doppler analysis of a microburst and its application to aircraft flight simulation. *J. Climate Appl. Meteor.*, 25, 1398-1425.

_____, 1982: Cell structure and evolution within a squall line as revealed by dual-Doppler radar. M. S., Thesis, University of Oklahoma, 212 pp.

Foote, G. B., and P. S. du Toit, 1969: Terminal velocity of raindrops aloft. *J. Appl. Meteor.*, 8, 249-253.

Frost, W., and Cheng, H., and Elmore, K. L., and McCarthy, John, 1984: Simulated Flight through JAWS Wind Shear: In Depth Analysis Results. *J. Aircraft*, 21, 797-802.

Fujita, T. T., 1985: The Downburst. *Satellite and Mesometeorology* (SMRP), University of Chicago, 51 pp.

_____, and Wakimoto, 1983: Microbursts in JAWS depicted by Doppler radars, PAM, and arial photographs. *Preprints, 21st Conf. on Radar Meteorology*, Edmonton, Canada, Amer. Meteor. Soc., 638-645.

_____, 1976: Spearhead echo and downburst near the approach end of a John F. Kennedy runway, New York City *SMRP.*, University of Chicago, 51 pp.

Gal-Chen, T., and R. A. Kropfli, 1984: Buoyancy and pressure perturbations derived from dual-Doppler radar observations of the planetary boundary layer: Applications for matching models with observations. *J. Atmos. Sci.*, 41, 3007-3020.

_____, 1982: Errors in fixed and moving frame of references: Applications for conventional and Doppler radar analysis. *J. Atmos. Sci.*, 39, 2279-2300.

_____, 1978: A method for the initialization of the anelastic equations. Implications for matching models with observations. *Mon. Wea. Rev.*, 106, 587-606.

Hane, C. E., and P. S. Ray, 1985: Pressure and buoyancy fields derived from Doppler radar data in a tornadic thunderstorm. *J. Atmos. Sci.*, 42, 18-35.

_____, R. B. Wilhelmson, and T. Gal-Chen, 1981: Retrieval of thermodynamic variables within deep convective clouds: Experiments in three dimensions. *Mon. Wea. Rev.*, 109, 564-576.

Hildebrand, P. H. and R. E. Carbone, 1980: Part V: Verification of Results, The Multiple Doppler Radar Workshop, Nov., 1979. Bull. Amer. Meteor. Soc. 61, 1189-1194.

Hjelmfelt, M. R., 1984: Radar and Surface Data Analysis of a Microburst in JAWS. Reprints, 22nd Conference on Radar Meteorology, Zurich, Switzerland, Amer. Meteo. Soc., 64-69.

_____, C. J. Kessinger, and Wilson, 1983: Low-level microburst wind structure using Doppler radar and PAM data. Preprints, 21st Conf. on Radar Meteor., Edmonton, Alta, Canada, Amer. Meteor. Soc., 602-608.

Hughes, R. G., 1986: Dynamic and thermodynamic characteristics of a microburst-producing storm in Colorado determined from JAWS dual-Dopppler data. Ph.D. Dissertation, St. Louis University, 214 pp.

Kessinger, C. J., P. S. Ray and C. E. Hàne, 1987: The Oklahoma squall line of 19 May 1977. Part I: A multiple Doppler analysis of convective and stratiform structure. J. Atmos. Sci., 44, 2840-2864.

_____, J. W. Wilson, M. Weisman, and J. Klemp, 1984: The evolution of misoscale circulations in a downburst-producing storm and comparison to numerical results, Preprints 22nd Conference on Radar Meteorology, Zurich, Switzerland, AMS, Boston, Mass., 58-63.

Lapointe, P. G. 1989: A sub-cloud layer vorticity budget analysis for two microburst-producing storms from JAWS dual-Doppler data. M. S., Thesis, St. Louis University, 89 pp.

Lin, Y. J., 1988: The Subcloud-layer eddy kinetic energy budget of a microburst-producing thunderstorm determined from JAWS dual-Doppler measurements, Boundary Layer Meteorology, 44, 349-357.

_____, and J. A. Coover, 1988: A kinetic energy analysis of a microburst-thunderstorm based on JAWS dual-doppler data. J. Atmos. Sci., 45, 2764-2771.

_____, and P. M. Condray, 1987: Momentum flux in the subcloud layer of a microburst producing thunderstorm determined from JAWS dual-Doppler data, Boundary Layer Meteorology, 43, 125-140.

_____, and R. G. Hughes, 1987: Structural features of a microburst-producing storm in Colorado revealed by JAWS dual-Doppler radars, J. Atmos. Sci., 44, 3640-3655.

———, ———, and R. W. Pasken, 1987: Subcloud-layer kinematic and dynamic structures of a microburst-producing thunderstorm in Colorado determined from JAWS dual-Doppler measurements. Boundary—Layer Meteorology, 39, 67-86.

———, and T. C. Wang, and J. H. Lin, 1986: Pressure and temperature perturbations within a squall-line thunderstorm Derived from SESAME dual-Doppler data, J. Atmos. Sci., 43, 2302-2326.

———, and R. W. Pasken, 1984: Dynamic and thermodynamic structures of a tornadic storm derived from Doppler winds, Papers in Meteor. Research, 7, Journal of the Meteorological Society of the Republic of China, 25-42.

Martner, B. E., 1975: Z-R and Z-W relations from dropsize measurements in high plains thunderstorms. Preprints, 9th Conf. on Severe Local Storms, Norman, Amer. Meteor. Soc., 307-310.

McCarthy, J., 1984: Recommendation for coping with microburst wind shear: An aviation hazard, J. of Air Law and Commerce, 49, 337-359.

———, and R. Serafin, 1984: The Microburst: Hazard to aviation, Weatherwise, 37, 120-127.

———, and Bedard, A., J., Jr., 1984: A Case study illustrating time scales and operational responses for a wind shear episode during the JAWS project. Preprints, 22nd Aerospace Sciences Meeting, Reno, Nev.

———, and J. Wilson, 1984: The Microburst as a hazard to aviation: Structure, mechanisms, climatology, and nowcasting. Preprints, Nowcasting II Symposium, Norrkoping Sweden, 21-30.

———, R. Roberts, and W. Schreiber, 1983: JAWS data collection, analysis highlights, and microburst statistics. Preprints, 21st Conf. on Radar Meteor., Edmonton, Alta., Canada, Amer. Meteor. Soc., 624-629.

McNamee, W. E., 1989: Examination of microburst development in a Colorado thunderstorm for the 5 August 1982 case. M. S. Thesis, St. Louis University, 151 pp.

Nelson, S. P., and R. A. Brown, 1982: Multiple doppler radar derived vertical velocities in thunderstorms. Part I-error analysis and solution techniques. NOAA Tech. Memo ERL-NSSL-94, 21 pp.

Parsons, D. B., R. A. Kropfli, J. M. Schmidt, and T. Gal-Chen, 1983:

Comparisons between Doppler radar derived air-motions in fixed and moving frames of reference. Preprints, 21st Conf. on radar Meteorology, Edmonton, Canada, Amer. Meteor. Soc., 558-564.

Pasken, R. W., and Y. J. Lin, 1982: Pressure perturbation within a tornadic storm derived from dual-Doppler wind data. Preprints, 12th Conf in Severe Local Storms, Amer. Meteor. Soc., 257-260.

Ray, P. S., C. L. Ziegler, W. Bumgarner, and R. J. Serafin, 1980: Single and multi-Doppler radar observations of tornadic storms. Mon. Wea. Rev., 108, 1607-1625.

_____, M. Gilet, and K. W. Johnson, 1980: Part IV: Motion field synthesis and radar placement, the multiple Doppler radar workshop, Nov., 1979,. Bull. Amer. Meteor. Soc., 61, 1184-1189.

_____, K. K. Wagner, K. W. Johnson, J. J. Stephens, W. C. Bumgarner, and E. A. Mueller, 1978: Triple-Doppler observations of a convective storm. J. Appl. Meteor., 17, 1201-1212.

Roux, F., J. Testud, M. Payen, and B. Pinty, 1984: West African squall-line thermodynamic structure retrieved from dual-Doppler radar observations. J. Atmos. Sci., 41, 3104-3121.

Srivastava, R. C., 1985: A simple model of evaporatively driven downdrafts: Application to microburst downdrafts. J. Atmos. Sci., 28, 1004-1023.

Wilson, J. R., and R. D. Roberts, C. Kessinger, and J. McCarthy, 1984: Microburst wind structure and evaluation of Doppler radar for airport wind shear detection. J. Climate Appl. Meteor., 22, 1227-1241.

_____, R. Carbone, H. Baynton, and R. J. Serafin, 1980: Operational application of meteorological Doppler radar, Bulletin American Meteorological Society, 61, 1154-1165.